Actinide opacities for modeling the spectra and light curves of kilonovae

C. J. Fontes[1,2*], C. L. Fryer[1,3,4,5,6], R. T. Wollaeger[1,3], M. R. Mumpower[1,7], and T. M. Sprouse[7]

[1] *Center for Theoretical Astrophysics, Los Alamos National Laboratory, Los Alamos, NM 87545, USA*
[2] *Computational Physics Division, Los Alamos National Laboratory, Los Alamos, NM 87545, USA*
[3] *Computer, Computational, and Statistical Sciences Division, Los Alamos National Laboratory, Los Alamos, NM 87545, USA*
[4] *Physics Department, University of Arizona, Tucson, AZ 85721, USA*
[5] *Physics and Astronomy Department, University of New Mexico, Albuquerque, NM 87131, USA*
[6] *The George Washington University, Washington, DC 20052, USA*
[7] *Theoretical Division, Los Alamos National Laboratory, Los Alamos, NM 87545, USA*

ABSTRACT

We extend previous ab initio calculations of lanthanide opacities (Fontes et al., 2020, MNRAS, 493, 4143) to include a complete set of actinide opacities for use in the modeling of kilonova light curves and spectra. Detailed, fine-structure line features are generated using the configuration-interaction approach. These actinide opacities display similar trends to those observed for lanthanide opacities, such as the lighter actinides producing higher opacity than the heavier ones for relevant conditions in the dynamical ejecta. A line-binned treatment is employed to pre-compute opacity tables for 14 actinide elements ($89 \leq Z \leq 102$) over a grid of relevant temperatures and densities. These tabular opacities will be made publicly available for general usage in kilonova modeling. We demonstrate the usefulness of these opacities in kilonova simulations by exploring the sensitivity of light curves and spectra to different actinide abundance distributions that are predicted by different nuclear theories, as well as to different choices of ejecta mass and velocity. We find very little sensitivity to the two considered distributions, indicating that opacities for actinides with $Z \geq 99$ do not contribute strongly. On the other hand, a single actinide element, protactinium, is found to produce faint spectral features in the far infrared at late times (5–7 days post merger). More generally, we find that the choice of ejecta mass and velocity have the most significant effect on KN emission for this study.

Key words: gravitational waves – opacity – radiative transfer – stars: neutron

1 INTRODUCTION

The effect of lanthanide opacities on the electromagnetic spectra produced during a kilonova (KN) event has been the focus of intense research over the past several years, as catalyzed by the recent KN observation associated with the gravitational wave detection known as GW170817 (Abbott et al. 2017a,b). The term kilonova (Li & Paczyński 1998; Kulkarni 2005; Metzger et al. 2010) refers to the electromagnetic radiation that can be produced after a neutron star merger (NSM). The emission from such events is powered by the radioactive decay of r-process elements that are created in this neutron-rich environment. High-energy photons, along with alpha particles, beta particles and fission fragments, produced during these decay events eventually thermalize, which leads to the thermal emission of radiation. The passage of thermal photons through, and possible escape from, the dynamical ejecta is expected to be controlled by the opacity of heavy elements that possess a large number (greater than 50) of bound electrons. These bound electrons are characterized by complex energy level diagrams and a corresponding, densely packed forest of bound-bound absorption (line) features

that can greatly inhibit the flow of photons through the dynamical ejecta. The atomic level populations, which are required to calculate the opaciy, are typically assumed to be in local thermodynamic equilibrium (LTE), at least during the early phase of a KN, i.e. less than about 7 days post merger.

While lanthanide opacities have been studied in some detail in this context, actinide opacities, which are the focus of this work, have been relatively ignored. The opacities of low-charge ion stages of actinide elements are expected to possess complex absorption features that are similar to those exhibited by the corresponding lanthanide elements. Furthermore, the production of actinides in NSMs remains an open topic of pursuit in nuclear physics (Wanajo et al. 2014; Wu et al. 2019; Vassh et al. 2020). For example, the synthesis of actinides may yield distinct gamma-ray emission from nascent fission fragments (Wang et al. 2020) or show unique imprints from the production of specific elements (Zhu et al. 2018; Korobkin et al. 2020), but large uncertainties in nuclear theory leave unresolved just how heavy an element can be created during these events (Mumpower et al. 2018; Côté et al. 2017; Möller et al. 2019).

As far as lanthanide elements are concerned, detailed line opacities were initially considered by Kasen et al. (2013), Tanaka & Hotokezaka (2013), Barnes & Kasen (2013) and Kasen et al. (2015) for

---

* E-mail: cjf@lanl.gov

use in KN simulations. An independent study (Fontes et al. 2015a, 2017) was carried out to investigate alternative methods of including detailed line opacities in KN modeling, i.e. the line-binned treatment considered in the present work. Subsequently, each of these three research groups produced a complete set of lanthanide opacities (Kasen et al. 2017; Fontes et al. 2020; Tanaka et al. 2020). Recent lanthanide opacity efforts have also focused on the calculation of precise atomic data (energies and radiative decay rates) that are used in the generation of opacities for KN modeling (Quinet & Palmeri 2020; Gaigalas et al. 2019; Radžiūtė et al. 2020; Carvajal Gallego et al. 2021, 2022).

As the analysis and understanding of GW170817 (and KNe in general) evolve, the need for detailed opacities has expanded beyond the lanthanide elements to include the fourth- through sixth-row elements of the periodic table. KN modelers now include opacities for these elements, as well as the lanthanides, to investigate an ever-growing list of applications, such as morphology and composition effects, specific line signatures for the purpose of elemental identification, non-LTE effects on the atomic level populations, and KN detectability studies, e.g. Kasen et al. (2017), Tanvir et al. (2017), Troja et al. (2017), Tanaka et al. (2018), Wollaeger et al. (2018), Kawaguchi et al. (2018), Watson et al. (2019), Wollaeger et al. (2019), Kawaguchi et al. (2020), Tanaka et al. (2020), Even et al. (2020), Banerjee et al. (2020), Bulla et al. (2021), Zhu et al. (2021), Korobkin et al. (2021), O'Connor et al. (2021), Gillanders et al. (2021), Domoto et al. (2021), Kawaguchi et al. (2021), Hotokezaka et al. (2021), Ristic et al. (2021), Chase et al. (2021), Wollaeger et al. (2021).

The purpose of the present work is to extend our earlier calculations of lanthanide opacites (Fontes et al. 2020, hereafter referred to as Paper I) to include the actinide elements. As noted in Fig. 1 of Paper I, the abundance of actinide elements is predicted to be similar to that of the lanthanides within the dynamical ejecta of a KN. To our knowledge, detailed actinide opacities have not been generated for KN modeling, with the exception of uranium, which we considered as the sole, representative actinide element in Paper I. (Those uranium opacity data are reproduced in the present work for completeness.) Here, we provide a complete set of frequency-dependent opacities for the actinide elements, and also demonstrate their usefulness in testing the sensitivity of KN spectra and light curves to different actinide abundance distributions that may arise due to variations in conditions or from large uncertainties predicted by current nuclear theory modeling (Sprouse et al. 2020; Côté et al. 2021).

2 ATOMIC PHYSICS CONSIDERATIONS

2.1 Basic considerations

The computational framework that is used to generate the actinide opacities in this work is the same as that described in Paper I, and so we provide a summary of our approach. We use the Los Alamos suite of atomic physics and plasma modeling codes (see Fontes et al. 2015b and references therein) to generate the fundamental atomic data, e.g. level energies, radiative decay rates, photoionization cross sections, as well as the LTE atomic level populations and resultant frequency-dependent opacities of interest.

The calculation of accurate, ab initio actinide energies and oscillator strengths for such a broad set of atomic levels and elements is very challenging, and is made more difficult by the paucity of benchmark values that are available compared to the lanthanides. So this dataset should be considered a first attempt to calculate a complete

set of actinide opacities. For this work, we chose the semi-relativistic Hatree-Fock capability within the Los Alamos suite because it provides a more complete description of the (non-local) electron-electron exchange potential compared to the (local-exchange) potential in the fully relativistic approach. The semi-relativistic approach also produces more physically reasonable results across the entire range of actinide elements. On the other hand, this approach lacks the relativistic physics that can be important to describe subtle, indirect effects concerning the $5f$ electrons that exist in neutral and low-charged actinide ions (Tatewaki et al. 2017; Rose et al. 1978).

From a computational perspective, the semi-relativistic calculations begin with the CATS atomic structure code (Abdallah et al. 1988), which employs the Hartree-Fock method of Cowan (Cowan 1981). These calculations produce detailed, fine-structure energy levels that include configuration interaction for the specified list of configurations (see Table A1). Oscillator strengths are also generated in this step, and are eventually used to produce the bound-bound contribution to the opacity. After the atomic structure calculations are complete, the GIPPER ionization code is used to obtain the relevant photoionization cross sections in the distorted-wave approximation. The photoionization data are used to generate the bound-free contribution to the opacity and are not expected to be too important for the present application, due to the range of relevant photon energies, but are included for completeness. Therefore, they are calculated in the configuration-average approximation, rather than fine-structure detail, in order to minimize the computational time.

The atomic level populations are calculated with the ATOMIC code from these fundamental atomic data. This code can be used in either LTE or non-LTE mode (Magee et al. 2004; Hakel & Kilcrease 2004; Hakel et al. 2006; Colgan et al. 2016; Fontes et al. 2016). The LTE approach was chosen for the present application, which requires only the atomic structure data, along with the temperature and density, to calculate the populations. The populations are then combined with the oscillator strengths and photoionization cross sections in ATOMIC to obtain the monochromatic opacities, which are constructed from the standard four contributions: bound-bound (b-b), bound-free (b-f), free-free (f-f) and scattering. Specific formulae for these contributions are readily available in various textbooks, such as Huebner & Barfield (2014).

To obtain the bound-bound contribution, we use the line-binned treatment described in Paper I. As this line-binned approach differs from the traditional expansion-opacity method (Sobolev 1960; Castor 1974; Karp et al. 1977), we provide a bit more detail on this topic. The expression for the (monochromatic) bound-bound contribution is given by

$$\kappa_\nu^{\mathrm{b-b}} = \frac{\pi e^2}{\rho m_e c} \sum_i N_i \left| f_i \right| L_{i,\nu} , \qquad (1)$$

where ν is the photon energy, ρ is the mass density, N_i is the number density of the initial level in transition i, f_i is the oscillator strength describing the photo-excitation of transition i, and $L_{i,\nu}$ is the associated line profile function. The corresponding line-binned, bound-bound opacities are comprised of discrete frequency (or wavelength) bins that contain a sum over all of the lines contained within a bin. An expression for this discrete opacity is obtained from the continuous opacity displayed in equation (1) by replacing the line profile with $1/\Delta\nu_j$, i.e.

$$\kappa_{\nu,j}^{\mathrm{bin}} = \frac{1}{\Delta\nu_j} \frac{\pi e^2}{\rho m_e c} \sum_{i \in \Delta\nu_j} N_i \left| f_i \right| , \qquad (2)$$

where $\Delta\nu_j$ represents the frequency width of a bin denoted by in-

teger index j. So, the summation encompasses all lines i with centers that reside in bin j. As in our previous work on lanthanides, we include only E1 dipole radiatiave transitions in the present models. Under LTE conditions, these allowed transitions are expected to provide the dominant contribution to the line absorption over a significant fraction of the energy range of interest. Forbidden transitions can produce weaker spectral features at relatively low photon energies, and a feasibility study of whether such features could be identified in observed KN spectra is a potential topic of future research.

As demonstrated in Paper I, simulated KN light curves produced with line-binned opacities are similar to those produced with the more commonly used expansion opacities, but specific spectral features can differ between the two methods, e.g. we observed that the expansion-opacity approach produced shallower absorption troughs. Furthermore, line-binned, bound-bound opacities have the advantage of being independent of the particular type of hydrodynamic expansion. Thus, one can pre-compute tabulated opacities on a grid of relevant temperatures and densities, thereby eliminating the need to explicitly calculate a large number of opacities during the radiation-transport portion of KN simulations.

2.2 Detailed considerations and comparisons

In this section, we discuss some convergence concepts associated with the calculation of atomic data and opacities. We also provide some comparisons to assess the accuracy of our atomic data.

From a general perspective, the ability to calculate large amounts of atomic data for actinide elements, with any significant accuracy, is a daunting theoretical challenge. It is well known that many "workhorse" atomic structure codes, such as the one currently employed, as well as others, are not expected to produce accurate transition energies and radiative rates for near-neutral ion stages of actinide elements without some sort of tuning, i.e. without the incorporation of some experimental data in order to improve ab initio calculations. As mentioned in the Introduction, the available benchmark data that can be used to evaluate the accuracy of our actinide calculations is rather scarce, which precludes the tuning approach. For the present application of KN modeling, this lack of accuracy is somewhat mitigated because the transport of radiation depends on the density of lines per energy (or wavelength) range in the opacity. From a theoretical perspective, many lines are summed within a given energy (or wavelength) bin to obtain their contribution to the opacity and then this quasi-continuum of lines is significantly smeared within the radiation-transport calculations due to the large velocity gradients, i.e. $\Delta v/c \sim 0.01$, that are predicted to occur in the dynamical ejecta of a KN. These considerations provide some justification for prioritizing completeness of the line contributions over accuracy of individual lines when calculating opacities for KN modeling. Thus, our strategy in the present, first attempt, is to produce atomic models that attempt to preserve the statistical nature of the myriad absorption features in actinide opacities.

2.2.1 Convergence discussion

Our method for generating lists of atomic configurations is similar to that employed in our previous work in Paper I on lanthanides. For a given ion stage, one starts with the ground configuration and then systematically considers single- and double-electron promotions to higher lying nl orbitals in order to form excited configurations. The relevant temperatures are sufficiently low for the KN modeling of

interest in this work (see Fig. 1 and the associated discussion in the next section) that one only needs to consider promotions from the valence orbitals, i.e. $5f$, $6d$, $7s$ subshells. The electron promotions are performed up to some maximum principal quantum number, $n_{\max}$, in order to ensure that that converged partition functions and level populations will be obtained from thermal considerations, i.e. based on Saha-Boltzmann statistics. The excited configurations must also permit all of the relevant dipole excitations from lower lying configurations whose fine-structure levels will contain significant populations. Additionally, these excited configurations must also be chosen such that enough configuration-interaction is included to produce reasonably converged level energies and radiative transition rates in the atomic structure calculations. Through trial and error, we found that a value of $n_{\max} = 7$ or 8 provides a reasonable balance between convergence and computational-resource considerations. Once a list of configurations is chosen, we perform fine-structure calculations based on those lists of configurations to obtain energy levels, wavefunctions and radiative decay rates. When then carry out some numerical convergence checks by extending the configuration lists using $n_{\max} + 1$, instead of $n_{\max}$. These tests indicate that the populations of low-lying atomic levels, which are responsible for producing the majority of lines, changed by a maximum of a few percent. So convergence with respect to atomic level populations is good. The spectral details of the opacities sometimes change in that additional lines appear at the very high and low ends in photon energy range of interest. However, these lines are not expected to contribute significantly to the KN modeling because: (1) At the high-energy end, the opacity is so large that the ejecta is already optically thick and adding additional lines would not change that condition. (2) At the low-energy end, the opacity is so small that the corresponding absorption and emission is typically too weak to contribute significantly to the KN simulations. These tests also sometimes reveal shifting in the energies and increases/decreases in the strengths of the lines that appear within the main photon energy range of interest, indicating that convergence with respect to configuration interaction is not complete. However, we mention that the qualitative behavior of the frequency-dependent opacities is very similar in these comparisons and the Planck mean opacities typically differ by less than 5–10%, which provides some confidence that the bulk, statistical properties of the forests of lines are preserved, even if the individual lines are not fully converged. A more extensive investigation of the configuration-list convergence is desirable for future work, in accord with similar statements made by Kasen et al. (2013) in the context of lanthanide opacity calculations.

2.2.2 Accuracy discussion

As in Paper I, for improved accuracy, we replace our calculated ionization potentials for the actinide elements with the values provided in the NIST Atomic Spectra Database (ASD) (Kramida et al. 2018). An illustrative example for this type of correction, is provied in Fig. 1 for uranium at a mass density of $\rho = 10^{-6}$ g/cm^3. We see that using NIST-corrected energies shifts the onset of the next higher ion stage to slightly higher temperatures. Similar figures (not shown) are obtained for the other actinides, due to the similarities in their ionization potentials for each ion stage. As mentioned in the previous section, this type of figure is also useful to estimate the maximum temperature at which each ion stage exists, which aids in the selection of appropriate list of configurations. This figure can also be used to estimate the maximum temperature of validity for the atomic models that are considered in this work. Since we only consider the first four ion stages of each element, the opacity cal-
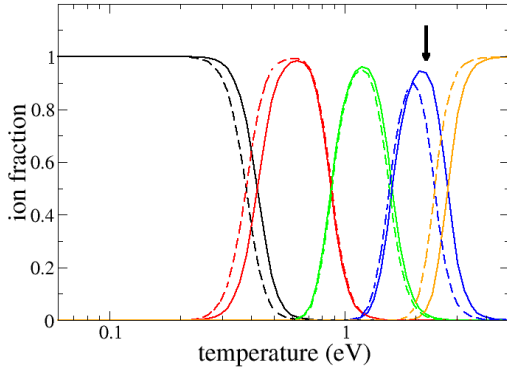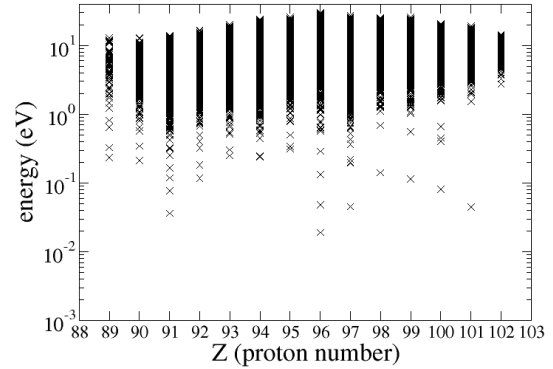
Figure 1. Ionization-stage fraction versus temperature for U at a typical mass density of $\rho = 10^{-6}$ g/cm^3. The black curves refer to U I, the red ones to U II, the green ones to U III, and the blue ones to U IV. The solid curves use NIST-corrected ionization energies (Kramida et al. 2018), while the dashed curves use uncorrected values. The vertical arrow, located at a temperature of about 2 eV, indicates the temperature above which the fraction of U V starts to become significant.

Figure 2. Calculated energy levels for the singly ionized stage of each actinide element. Each energy level is represented by an × symbol.

Table 1. A tabular display of whether the present calculations predict the same ground state as that listed in the NIST Atomic Spectra Database (Kramida et al. 2018). Each row contains assessment codes for the four ion stages associated with a particular actinide element, which is labeled by its Z value in the first column. A checkmark indicates that our calculations match the NIST result. An integer indicates a mismatch in the predicted level and denotes the level number in our list of energy-ordered levels (for that ion stage) that corresponds to the NIST label.

Z	assessment code			
89	✓	✓	2	✓
90	✓	3	3	✓
91	2	10	12	✓
92	✓	6	7	✓
93	✓	✓	3	✓
94	✓	3	✓	✓
95	✓	✓	✓	✓
96	✓	2	3	✓
97	✓	2	✓	✓
98	✓	✓	✓	✓
99	✓	✓	✓	✓
100	✓	✓	✓	✓
101	✓	✓	✓	✓
102	✓	✓	✓	✓

culations are expected to be valid up to a maximum temperature of $T \sim 2$ eV (23 kK), as indicated by the vertical arrow in Fig. 1. Going to higher temperatures would require the inclusion of additional ion stages in the models.

While the actinide data in the NIST database is not plentiful, there is one quantity that is readily available for each ion stage of every actinide element, the level label of the predicted ground state. We display in Table 1 a simple comparison of this information. For a given ion stage, a checkmark indicates that our calculations predict the same ground level as the one in the NIST database. An integer indicates a mismatch in the predicted level and denotes the level number in our list of energy-ordered levels (for that ion stage) that

corresponds to the NIST label. We see that our ab initio calculations are not perfect, but they match the NIST label 77% of the time. When there is a mismatch, the NIST ground level is often a relatively low-lying level in our calculations, i.e. the second or third level. However, our code displays stronger mismatches for the second and third ion stages of $Z = 91$, protactinium, and moderate mismatches for the same ion stages of $Z = 92$, uranium, illustrating the challenges of calculating the entire range of actinide elements within a single, self-consistent framework. These mismatches could likely be improved by tuning our atomic structure calculations, but such manipulations do not necessarily result in more accurate values of the excited-state energies, and so we prefer to use a consistent, ab initio approach in the present work.

Before providing a comparison of more refined atomic data, we offer a simple visual inspection of the trends in our level energies. In Fig. 2, we display our excited-state energies for the singly charged ion stages, in a schematic format. As expected from basic atomic theory, there is some visible left-right symmetry about the $Z = 95$ column, which is characterized by a ground state that contains a half-filled $(5f^7)$ f shell. From energy-minimization and angular-momentum-coupling considerations, ion stages that contain ground states with half-filled subshells are expected to (1) be semi-stable, i.e. a larger energy gap between the ground and first excited states compared to adjacent ion stages, and (2) contain more excited states due to the coupling of 7 electrons in an f subshell. This symmetry is not as strong as that exhibited in the corresponding lanthanide diagram, which might be an indication of a difference in electron correlation effects in actinides compared to lanthanides. Or it could indicate a lack of accuracy in the atomic structure calculations of the singly ionized actinides.

Continuing with the discussion of excited-state energies, in Fig. 3 we present the energies for the neutral stage of each actinide element. There is less symmetry in this figure compared to that displayed in the previous Fig. 2 for the singly ionized ions, with a noticeable lack of lower-lying excited states for the rightmost five elements. Since there is no obvious reason for this pattern, it is likely an indication of a lack of accuracy in the calculations for these neutral cases, which is not surprising from a theoretical perspective. In general, the neutral stage of an element is the most difficult to calculate in an accurate manner due to the existence of valence electrons that are only lightly bound to the nucleus, and so it becomes important to calculate the electron-electron interaction with higher
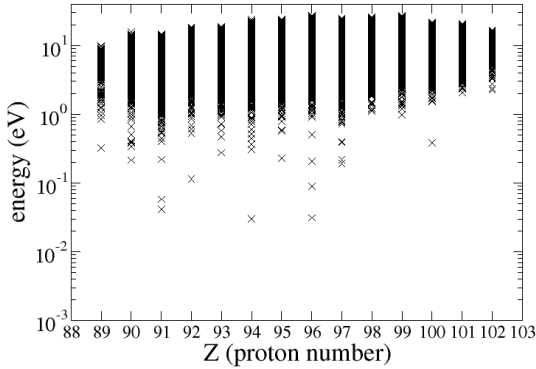
Figure 3. Calculated energy levels for the neutral stage of each actinide element. Each energy level is represented by an × symbol.

than usual precision. These neutral calculations for lanthanides can pose significant numerical, even for the accurate multiconfiguration Dirac-Hartree-Fock (MCDHF) method (Grant 2007; Gaigalas et al. 2019).

Next, we provide comparisons between our calculated results and the line data that are available in the NIST database. Some line information is available for the first 11 actinides. Of those 11, only the first one, actinium ($Z = 89$), contains both transition rates and level designations, which is the most useful type of information for providing a meaningful accuracy assessment. NIST data are available for the first three ion stages of Ac, and so we provide a comparison of those results in Table 2. In these comparisons, we consider all of the available NIST data for Ac III, but limit the comparisons for Ac I and Ac II in the interest of brevity and also due to the labor-intensive process required to match the level designations between the present and NIST data sets. Not surprisingly, the labels do not appear in the same energy order, and the appearance of duplicate labels (due to the complexity of the angular momentum coupling) makes it challenging to make clear matches. Sometimes, an inspection of the mixing purity ("Leading percentages") quantity is also required in order to make a definitive identification, if such information is provided. Thus, for Ac I we considered only those radiative transitions with a lower level of the first excited state, $6d\,7s^2\,{}^2D_{5/2}$, which is predicted to lie only 0.277 eV above the $6d\,7s^2\,{}^2D_{3/2}$ ground state, according to the NIST database. We chose the first excited state, rather than the ground state, because the NIST database includes a $6d - 5f$ transition for the excited state, while no such transitions are provided for the ground state. For Ac II we chose two lower levels, the ground and first excited states, in order to highlight the various types of orbital transitions. Despite these constraints, the comparisons in Table 2 provide a representative sample of the accuracy for the various types of radiative transitions in our Ac model.

Starting with the highest charged ion stage, Ac III, which is expected to be the most accurately calculated, we see that the transition energies agree well (within 6%) for the the first five transitions, which are of the type $6d - 7p$ and $7s - 7p$. On the other hand, the energies for the remaining three transitions, which are of the type $6d - 5f$, differ by about 30%, indicating the difficulty in accurately calculating the $5f$ wavefunction with the semi-relativistic approach. The radiative decay rates follow a similar trend, with the first five transitions showing differences of 27–57%, while the last three transitions display significantly larger differences, i.e. greater

than a factor of four. For convenience, we have also provided the letter codes for the NIST accuracy estimate in the final column of the table. These codes range from AAA ($< 0.3\%$) to E ($> 50\%$). (See the NIST website for a full listing of accuracy codes.) All eight transitions for Ac III are rated B+, which indicates an accuracy of $\leq 7\%$. Thus, all of the calculated rates fall outside of the NIST estimated accuracy for this ion stage.

Moving on to Ac II, the five transitions with the ground state as the lowest level display differences in the transition energies ranging from 4–14%. The fourteen transitions with the first excited state as the lowest level display similar differences, ranging from 0.1–18%. The decay rates show a broad range of differences, ranging from 5.6% to a factor of 3.17. A number of the calculated rates fall within the NIST accuracy estimate, but not all of them. We also note that the calculated energies and decay rates are sometimes higher, and sometimes lower, than the NIST values, indicating a lack of a systematic shift in the calculated data.

Finally, we consider the 29 transitions within the neutral stage, Ac I, with the first excited state as the lower level. The comparisons for this ion stage display the largest disagreements. The transition energy differences range from 0.5–30%. The radiative decay rates differ by as little as 6%, while a factor of about 10 is obtained for two of the transitions. A few of the calculated rates fall within the NIST accuracy estimate, but most do not. As in the case of the singly ionized stage, there does not appear to be a systematic (upward or downward) shift in the calculated data relative to the NIST data.

3 SAMPLE OPACITIES AND TABLES

In this section, we provide some example opacities and information concerning the tabular opacities that are generated for KN simulations. The content presented here is similar to that provided in Section 3 of Paper I and is, therefore, presented in a more concentrated, abbreviated form.

In order to illustrate the basic characteristics of the opacities used in this study, we present in Fig. 4 the monochromatic opacity of U for typical ejecta conditions of $T = 0.5$ eV and $\rho = 10^{-13}$ g/cm^3. The solid black curve displays the complete (or total) opacity, with all four contributions (b-b, b-f, f-f and scattering), while the dashed red curve shows the contributions that arise only from free electrons (f-f and scattering) in order to highlight the massive differences that can occur when the bound electrons are taken into account. The b-b contribution was calculated via the line-binned expression in equation (2). The f-f and scattering contributions were obtained from the simple, analytic formulae (Huebner & Barfield 2014) associated with Kramers and Thomson, respectively. The gap between the b-b features and the onset of the b-f edges occurring at $\sim$ 10–20 eV is due to missing lines that would be present if more excited configurations had been included in the model. (Our transport calculations have minimal intensity at these energies.) We note that a mean charge state of $\overline{Z} = 1.995$ is obtained for these conditions, indicating that the opacity is dominated by U III, or doubly ionized uranium.

3.1 Examples of line-binned opacities

To illustrate how the opacities behave as a function of element, we present a complete set of actinide opacities at a characteristic ejecta density of $\rho = 10^{-13}$ g/cm^3 in Fig. 5. In this case, a temperature of $T = 0.3$ eV was chosen in order to highlight opacities with a b-b

Table 2. A comparison of our calculated energy levels and radiative transition rates with data available in the NIST database. Comparisons are provided for the first three ion stages of Ac ($Z = 89$). The NIST accuracy estimate code is listed in the final column. (See text for details.)

lower level	upper level	transition energy (eV) NIST	Present	radiative decay rate (s^{-1}) NIST	present	ratio of decay rates (present/NIST)	accuracy estimate
				Ac I			
$6d7s^2\ ^2D_{5/2}$	$6d^27p\ ^4D_{5/2}$	4.0204406	4.00	3.5E+07	5.57E+06	0.159	E
$6d7s^2\ ^2D_{5/2}$	$7s^25f\ ^2F_{7/2}$	3.9834653	4.19	1.1E+08	2.25E+07	0.205	D+
$6d7s^2\ ^2D_{5/2}$	$6d^27p\ ^2F_{7/2}$	3.9086043	3.96	4.9E+07	4.43E+07	0.904	D+
$6d7s^2\ ^2D_{5/2}$	$7s^25f\ ^2F_{5/2}$	3.8983382	4.19	1.5E+07	2.08E+06	0.139	D+
$6d7s^2\ ^2D_{5/2}$	$6d^27p\ ^4S_{3/2}$	3.8047011	4.06	—	8.54E+06	—	—
$6d7s^2\ ^2D_{5/2}$	$6d^27p\ ^4D_{3/2}$	3.7522887	3.70	—	2.23E+06	—	—
$6d7s^2\ ^2D_{5/2}$	$6d^27p\ ^2F_{5/2}$	3.6660786	3.84	—	1.20E+06	—	—
$6d7s^2\ ^2D_{5/2}$	$6d^27p\ ^2D_{5/2}$	3.6281802	4.00	6.6E+07	6.57E+06	0.0995	D+
$6d7s^2\ ^2D_{5/2}$	$6d^27p\ ^4D_{3/2}$	3.4920317	3.82	1.3E+07	4.21E+06	0.324	E
$6d7s^2\ ^2D_{5/2}$	$6d^27p\ ^4F_{7/2}$	3.265365	3.45	8.E+06	9.78E+05	0.122	D+
$6d7s^2\ ^2D_{5/2}$	$6d6s7p\ ^2F_{7/2}$	3.1899927	2.79	1.1E+08	1.90E+08	1.723	D+
$6d7s^2\ ^2D_{5/2}$	$6d^27p\ ^4F_{5/2}$	3.0721332	3.30	3.7E+07	3.49E+06	0.0943	D+
$6d7s^2\ ^2D_{5/2}$	$6d7s7p\ ^2F_{5/2}$	3.0506018	2.60	—	1.99E+07	—	—
$6d7s^2\ ^2D_{5/2}$	$6d^27p\ ^4F_{3/2}$	3.0130314	3.17	—	9.74E+05	—	—
$6d7s^2\ ^2D_{5/2}$	$6d^27p\ ^2D_{5/2}$	2.9551157	2.81	1.0E+08	1.71E+08	1.71	D+
$6d7s^2\ ^2D_{5/2}$	$6d7s7p\ ^2P_{3/2}$	2.8191355	2.61	7.2E+07	7.64E+07	1.06	D+
$6d7s^2\ ^2D_{5/2}$	$6d7s7p\ ^2F_{7/2}$	2.7774347	2.46	4.1E+07	3.00E+07	0.732	D+
$6d7s^2\ ^2D_{5/2}$	$6d^27p\ ^2D_{3/2}$	2.6886477	2.44	—	1.46E+07	—	—
$6d7s^2\ ^2D_{5/2}$	$6d^27p\ ^4G_{5/2}$	2.6864196	2.90	1.1E+07	8.63E+06	0.785	E
$6d7s^2\ ^2D_{5/2}$	$6d^27p\ ^4G_{7/2}$	2.6339837	3.09	5.E+06	1.42E+07	2.84	E
$6d7s^2\ ^2D_{5/2}$	$6d7s7p\ ^4P_{5/2}$	2.5503147	2.06	—	2.23E+05	—	—
$6d7s^2\ ^2D_{5/2}$	$6d7s7p\ ^2F_{5/2}$	2.3512907	2.21	1.6E+07	2.25E+07	1.41	D+
$6d7s^2\ ^2D_{5/2}$	$6d7s7p\ ^2D_{3/2}$	2.0805811	1.75	—	2.08E+04	—	—
$6d7s^2\ ^2D_{5/2}$	$6d7s7p\ ^2D_{5/2}$ or $^4D_{5/2}$	1.948942	1.62	7.6E+06	2.77E+06	0.364	B
$6d7s^2\ ^2D_{5/2}$	$6d7s7p\ ^4D_{3/2}$	1.9223543	1.53	7.7E+05	9.97E+04	0.129	C
$6d7s^2\ ^2D_{5/2}$	$6d7s7p\ ^4F_{7/2}$	1.9158584	1.58	1.18E+06	7.01E+05	0.594	C+
$6d7s^2\ ^2D_{5/2}$	$6d7s7p\ ^4F_{5/2}$	1.5757503	1.30	1.56E+06	9.36E+05	0.600	C+
$6d7s^2\ ^2D_{5/2}$	$6d7s7p\ ^4F_{3/2}$	1.4235204	1.17	1.7E+05	4.35E+04	0.256	C
$6d7s^2\ ^2D_{5/2}$	$7s^27p\ ^2P_{3/2}$	1.2454607	0.958	3.56E+06	2.54E+06	0.713	B+
				Ac II			
$7s^2\ ^1S_0$	$6d7p\ ^1P_1$	5.480092	5.26	—	5.72E+08	—	—
$7s^2\ ^1S_0$	$6d7p\ ^3P_1$	4.5694975	4.03	2.5E+07	5.48E+07	2.19	E
$7s^2\ ^1S_0$	$6d7p\ ^3D_1$	4.139654	3.67	1.6E+08	1.69E+08	1.056	E
$7s^2\ ^1S_0$	$6d7p$ or $7s7p\ ^1P_1$	3.6265838	3.19	1.2E+08	1.09E+08	0.908	E
$7s^2\ ^1S_0$	$7s7p\ ^3P_1$	2.750035	2.42	2.13E+07	1.26E+07	0.591	B
$6d7s\ ^3D_1$	$5f6d\ ^1D_2$	4.9551105	5.84	—	8.79E+06	—	—
$6d7s\ ^3D_1$	$5f6d\ ^3F_2$	4.5674445	5.27	3.4E+07	5.70E+07	1.68	E
$6d7s\ ^3D_1$	$6d7p\ ^3P_2$	4.1698345	4.02	—	1.54E+07	—	—
$6d7s\ ^3D_1$	$6d7p\ ^3P_1$	3.981858	3.79	2.4E+08	1.26E+08	0.525	D+
$6d7s\ ^3D_1$	$6d7p\ ^3P_0$	3.9725015	3.74	4.E+08	3.79E+08	0.948	E
$6d7s\ ^3D_1$	$6d7p\ ^3F_2$	3.8010436	4.46	1.7E+08	3.24E+08	1.91	E
$6d7s\ ^3D_1$	$6d7p\ ^3D_1$	3.5520145	3.43	1.0E+08	1.49E+08	1.49	D+
$6d7s\ ^3D_1$	$6d7p\ ^3D_2$	3.5416468	3.49	—	3.31E+07	—	—
$6d7s\ ^3D_1$	$6d7p\ ^1D_2$	3.3648353	3.36	1.0E+07	3.17E+07	3.17	E
$6d7s\ ^3D_1$	$6d7p\ ^1P_1$	3.0389443	2.95	—	1.21E+07	—	—
$6d7s\ ^3D_1$	$7s7p\ ^3P_2$	2.9088535	2.69	—	6.93E+06	—	—
$6d7s\ ^3D_1$	$6d7p\ ^3F_2$	2.6913618	2.75	2.6E+07	3.99E+07	1.53	D+
$6d7s\ ^3D_1$	$7s7p\ ^3P_1$	2.1623955	2.18	1.04E+07	1.13E+07	1.09	B
$6d7s\ ^3D_1$	$7s7p\ ^3P_0$	2.0106255	2.05	2.80E+07	3.59E+07	1.28	B
				Ac III			
$6p^67s\ ^2S_{1/2}$	$6p^67p\ ^2P_{3/2}$	4.719214	4.51	3.97e+08	5.04E+08	1.27	B+
$6p^66d\ ^2D_{3/2}$	$6p^67p\ ^2P_{3/2}$	4.619904	4.60	2.89e+07	4.52E+07	1.56	B+
$6p^66d\ ^2D_{5/2}$	$6p^67p\ ^2P_{3/2}$	4.197993	4.13	2.30e+08	2.93E+08	1.27	B+
$6p^67s\ ^2S_{1/2}$	$6p^67p\ ^2P_{1/2}$	3.653305	3.67	1.90e+08	2.74E+08	1.44	B+
$6p^66d\ ^2D_{3/2}$	$6p^67p\ ^2P_{1/2}$	3.553995	3.77	1.58e+08	2.49E+08	1.57	B+
$6p^66d\ ^2D_{3/2}$	$6p^65f\ ^2F_{5/2}$	2.808675	3.62	1.85e+07	8.81E+07	4.76	B+
$6p^66d\ ^2D_{5/2}$	$6p^65f\ ^2F_{7/2}$	2.712320	3.51	2.11e+07	8.56E+07	4.06	B+
$6p^66d\ ^2D_{5/2}$	$6p^65f\ ^2F_{5/2}$	2.386764	3.14	8.79e+05	4.12E+06	4.69	B+
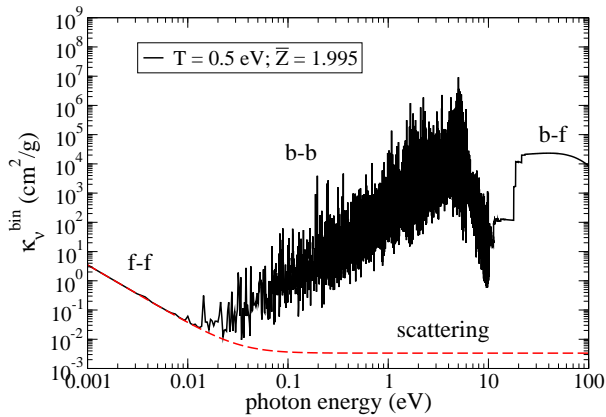
Figure 4. The LTE line-binned opacity for uranium at $T = 0.5$ eV and $\rho = 10^{-13}$ g/cm^3. The solid black curve displays the complete (or total) opacity, which includes the bound-bound, bound-free, free-free and scattering contributions. The dashed red curve displays only the contributions due to free electrons, i.e. the free-free and scattering contributions. The average charge state, $\overline{Z}$, for these conditions is listed in the legend.

contribution that is dominated by the second, i.e. singly ionized, ion stage of each element.

The qualitative trends in the various panels of this figure strongly resemble those presented in the corresponding plot (Fig. 7) of Paper I for the singly ionized lanthanides. For example, the bound-bound features generally increase in strength with photon energy for each element, peaking at about 3 eV, indicating that the emission of photons in the visible range would be strongly suppressed for these conditions. However, as in the case of lanthanide opacities, there are important quantitative differences in these detailed line-binned features when comparing one element to another, which we illustrate in Fig. 6. In each of the two panels in Figure 6, the solid black curve (with circles) represents the number of lines in the second ion stage, which is the dominant stage for these conditions, for each element. The number of lines for the various ion stages can also be found in Table A1. Superimposed on this black curve is a red dashed curve (with squares) that represents the mean opacity obtained from the frequency-dependent opacities in Figure 5. The red dashed curve in the left panel represents the Planck mean opacity, while the red dashed curve in the right panel represents the Rosseland mean opacity.

As expected, the number of lines reaches a maximum near the center of the actinide range (occuring at Cm II in this example), due to the presence of a ground-state configuration with a $5f^7$ sub-shell. This half-filled subshell produces the maximum number of fine-structure levels, compared to other ground-state configurations with different $5f$ occupation numbers, due to the rules of quantum mechanics and angular momentum coupling. Also as expected from the lanthanide-opacity analysis in Paper I, the mean-opacity curves display some structure, rather than near-constant behavior, illustrating that there exist significant differences in the detailed line structures for each element.

In fact, both opacity curves indicate relatively high mean values for the first half of the actinide range, followed by a local minimum near the center of the actinide range, and then a strong monotonic decrease over the latter half of the range. These trends are very similar to those exhibited by the singly ionized lanthanides in Fig. 9 of Paper I. The high values over the first part of the range indicate that the energy-level spacings of the low-lying levels of these actinides are conducive to the absorption of photons in relevant energy ranges for KN modeling. On the other hand, the monotically decreasing behavior indicates that the latter half of the actinides should not be as effective at absorbing photons.

We also note that this elemental sensitivity is consistent with previous studies of KN emission sensitivity to the lanthanide opacities (Even et al. 2020; Tanaka et al. 2020) in which it was shown that Nd has an outsize effect due to the energy positions and strengths of its line absorption features compared to the other lanthanides. The effect of U was also studied by Even et al. 2020, as it was the sole, representative actinide in that work, and it was found to have a similar outsize effect on KN emission. This common behavior of Nd and U is expected because these two elements are homologues, with low-lying energy levels containing $4f$ and $5f$ electrons, respectively.

3.2 Opacity tables

In order to perform radiation-transport calculations in an efficient manner, opacity tables were generated for the 14 actinide elements discussed above, using prescribed temperature and density grids that span the range of conditions of interest. The temperature grid consists of 27 values (in eV): 0.01, 0.07, 0.1, 0.14, 0.17, 0.2, 0.22, 0.24, 0.27, 0.3, 0.34, 0.4, 0.5, 0.6, 0.7, 0.8, 0.9, 1.0, 1.2, 1.5, 2.0, 2.5, 3.0, 3.5, 4.0, 4.5, and 5.0. (As mentioned in Section 2.2, the present models are only valid up to $T \sim 2$ eV, due to the inclusion of just the first four ion stages in the atomic physics calculations.) The density grid contains 17 values ranging from 10^{-20} to 10^{-4} g/cm^3, with one value per decade. Our photon energy grid is the same 14,900-point grid that is used in standard Los Alamos tabular opacity efforts, e.g. Colgan et al. 2016. The grid is actually a temperature-scaled $u = h\nu/kT$ grid with a non-uniform spacing that is designed to provide accurate Rosseland and Planck mean opacities. A description of this grid is available in Table 1 of Frey et al. 2013.

4 INVESTIGATION OF ACTINIDE OPACITIES IN THE MODELING OF LIGHT CURVES AND SPECTRA

In this section, we explore the effect of actinide opacities on the modeling of KN light curves and spectra. We are particularly interested in searching for spectral signatures that could be used to distinguish between differing actinide abundances in the dynamical ejecta. Such distinctions may provide unique insight into the relevant nuclear properties unreachable by current facilities (Mumpower et al. 2016a; Horowitz et al. 2019).

In order to be consistent with our previous investigation of lanthanide opacities, we first consider the KN model described in Section 4.2 of Paper I, i.e. a dynamical ejecta with a mass of 1.4×10^{-2} M$_\odot$ and mean ejecta speed of $0.125c$ (maximum speed of $0.25c$). Based on the spectral results from those simulations, we next expand our study to consider a broader range of conditions using a prescribed grid of three ejecta masses and three speeds. For all of the light-curve and spectral simulations that follow, we consider dynamical ejecta with the "main" r-process elemental abundance pattern described in Even et al. 2020 (see, for example, Fig. 1 therein), with the total actinide mass fraction held fixed at a value of 0.0884. However, we allow the abundances for the individual actinides to vary according to the three distributions described below. Although
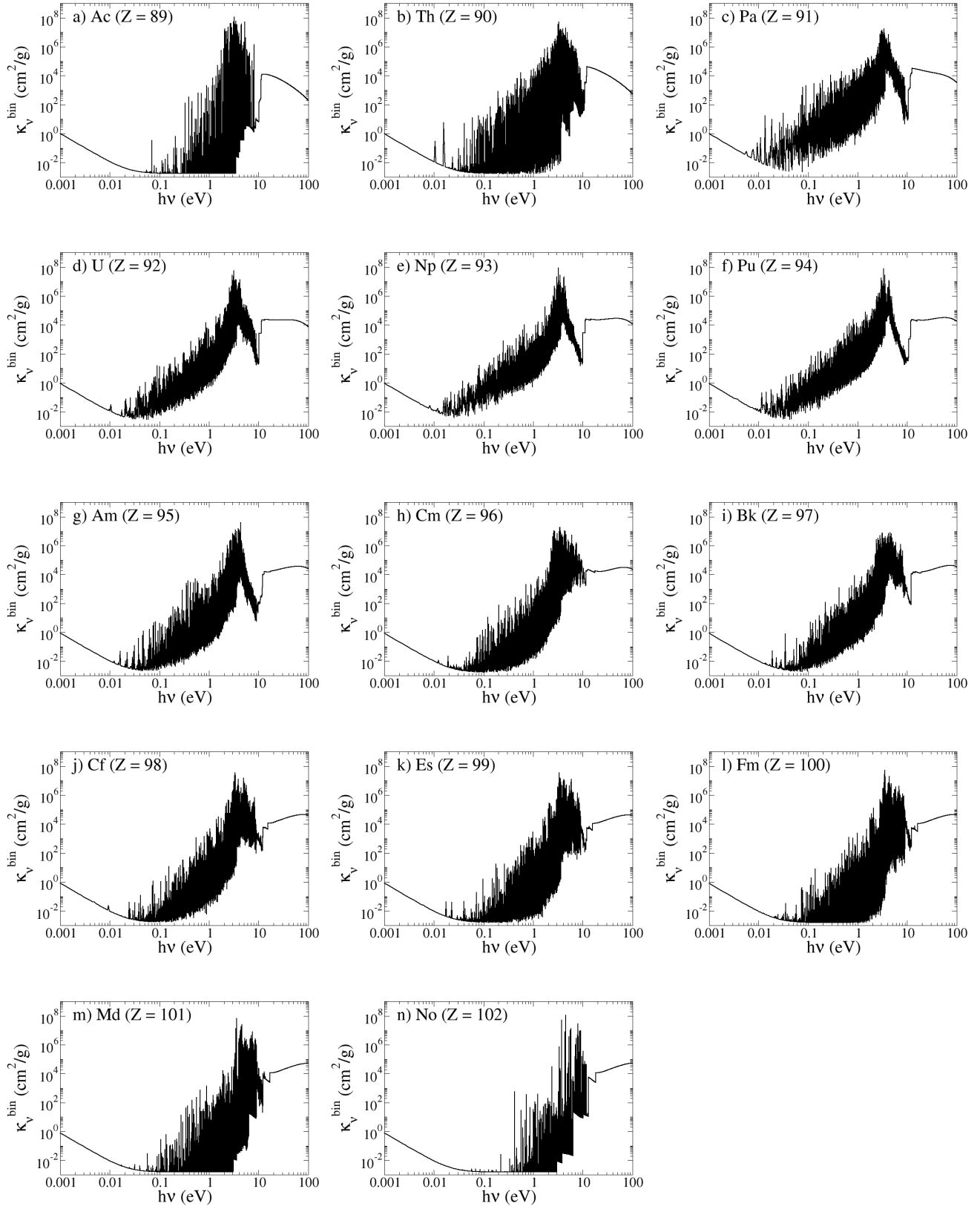
Figure 5. The LTE line-binned opacity for all 14 actinide elements at $T = 0.3$ eV and $\rho = 10^{-13}$ g/cm^3. For these conditions, the bound-bound contribution to the opacity is dominated by the second, i.e. singly ionized, ion stage of each element. Panels a–n display results for $Z = 89$–102 in numerical order.
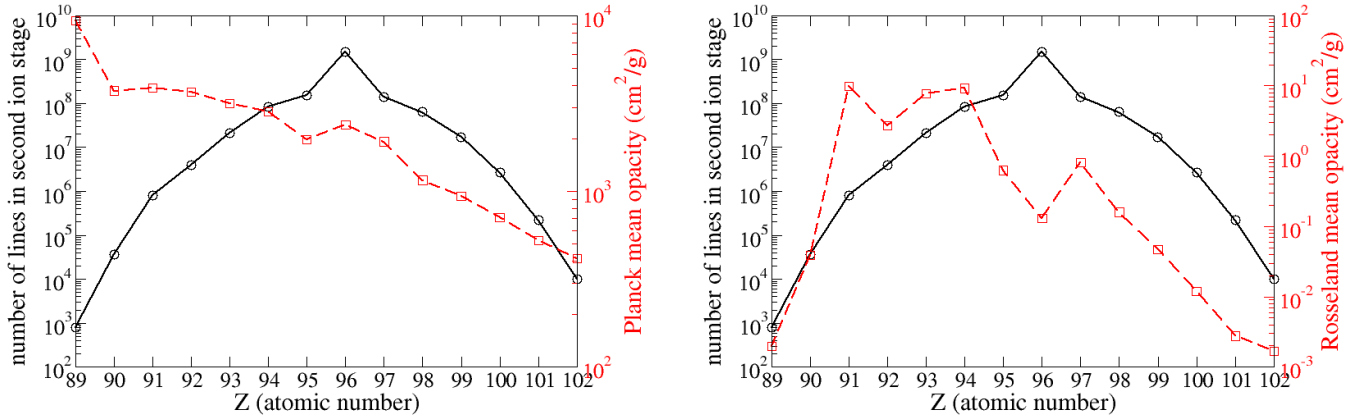
Figure 6. The number of lines in the second ion stage versus atomic number, Z (see, also, Table A1). The mean opacity associated with the line-binned opacities presented in Fig. 5 is also plotted versus Z. Results are presented for all 14 actinide elements ($Z = 89$–102). In both panels, the number of lines for the second ion stage is represented by the black solid curve (with circles). This curve is associated with the left-hand y axis in each panel. The red dashed curves (with squares), assocated with the right-hand y axis in each panel, represent the Planck mean opacity in the left panel and the Rosseland mean opacity in the right panel. The mean opacities were calculated at $T = 0.3$ eV and $\rho = 10^{-13}$ g/cm^3, corresponding to the conditions used in Fig. 5.

we alter the abundance fractions, we assume that the nuclear heating rate associated with the r-process elements is chosen to be the same for all models, following the prescription described in Wollaeger et al. (2018). As in the case of Paper I, the radiative transfer for these simulations is carried out with the Monte Carlo code SuperNu (Wollaeger & van Rossum 2014), with some improvements to the accuracy of the discrete diffusion optimization. The span of wavelength simulated is 1,000 to 128,000 Å with 1,024 logarithmically spaced groups (see Paper I for details).

To estimate the range of actinide production, we perform an r-process nucleosynthesis simulation with Portable Routines for Integrated nucleoSynthesis Modeling (PRISM) (Mumpower et al. 2017; Vassh et al. 2019) using a NSM trajectory indicative of typical, very neutron rich (low electron fraction) dynamical ejecta (Piran et al. 2013; Korobkin et al. 2012; Rosswog et al. 2013). Actinide production is sensitive to a variety of nuclear model inputs Mumpower et al. (2016b). To provide a range of possible outcomes, we consider several state-of-the-art predictions in this work. For masses, we use KTUY Koura et al. (2005), FRDM2012 Möller et al. (2016), HFB-17 Goriely et al. (2009), and UNEDF1 Kortelainen et al. (2012). All other properties are computed self-consistently with the masses according to the prescription of Ref. Mumpower et al. (2015). Neutron capture rates are computed with the CoH$_3$ statistical Hauser-Feshbach code Kawano et al. (2016); Mumpower et al. (2017). Beta-decay rates are based on the strength data of Möller et al. (2019), and delayed neutron emission is computed with the coupled Los Alamos Quasi-particle Random Phase Approximation plus Hauser-Feshbach code Mumpower et al. (2016c). Fission barriers are consistent with the mass model used, respectively, Koura (2014); Möller et al. (2015); Goriely et al. (2007), except in the case of the UNEDF1 model, as no fission barriers are available. In this case, we use the barriers of Ref. Möller et al. (2015). Spontaneous, β-delayed and neutron-induced fission channels are considered as in previous work Zhu et al. (2018); Mumpower et al. (2018); Vassh et al. (2020); Sprouse et al. (2021). Theoretical alpha decays of the heaviest nuclei are estimated using the Viola-Seaborg relation and depend on the masses Viola & Seaborg (1966). Evaluated data are taken
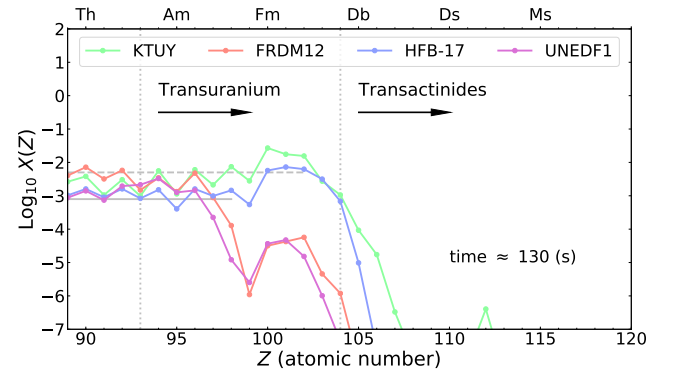
Figure 7. The range of actinide and transactinide element production in dynamical ejecta using a variety of nuclear models. The quantity $X(Z)$ is the mass fraction of an element with atomic number Z. The two horizontal gray lines illustrate the simplified distributions that are considered in this work: the solid gray line corresponds to a uniform distribution for actinides with $Z = 89$–98 and the dashed gray line corresponds to a uniform distribution for $Z = 89$–102.

where available from the Atomic Mass Evaluation (2016) Wang et al. (2017) and NuBase (2016) Audi et al. (2017).

Fig 7 shows the resultant range of actinide and transactinide elemental mass fractions, $X(Z)$, during this simulation. These curves were generated with a variety of nuclear models (Koura et al. 2005; Möller et al. 2016; Goriely et al. 2009; Kortelainen et al. 2012). These nuclear abundances change in time due to α-decay, β-decay and spontaneous fission (Zhu et al. 2018). Based on the Z dependence of the curves in this figure, we chose to simplify our analysis in this work by considering the following three static-abundance distributions: pure U (to be consistent with the analysis by Even et al. (2020)), a uniform distribution of actinides within the limited range of $Z = 89$–98 (which corresponds to the FRDM12 and UNEDF1 models in Fig. 7), and a uniform distribution of actinides encompassing the entire range of $Z = 89$–102 (similar to KTUY and
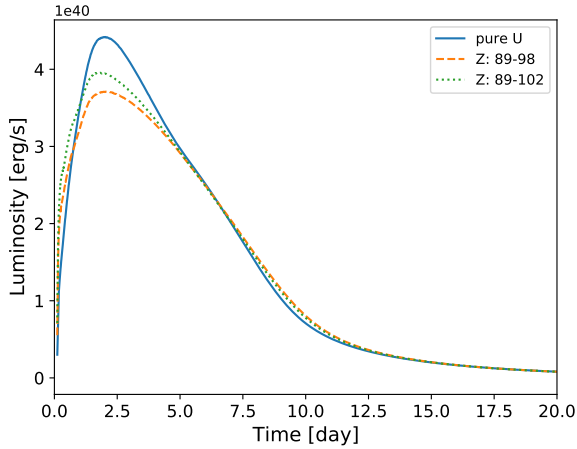
Figure 8. Bolometric luminosity for the first dynamical ejecta model, with a mass of 1.4×10^{-2} M$_\odot$ and mean ejecta speed of 0.125c. Results are displayed for three different actinide abundance distributions: pure U (solid blue curve), a uniform distribution including only a limited range of actinides from $Z = 89–98$ (dashed orange curve), and a uniform distribution including the entire range of actinides from $Z = 89–102$ (green dotted curve).

HFB-17 in Fig. 7). The latter two distributions may arise if the fission barrier heights are locally large in this region, leading to a robust production of actinides during a merger event (Holmbeck et al. 2019a,b). For convenience, these two uniform distributions are illustrated in Fig. 7 by (solid and dashed) horizontal gray lines, which differ in value by a ratio of 10/14.

4.1 Emission study using a single ejecta mass and speed

As mentioned above, in order to investigate the effect of the three different actinide distributions, we first consider the KN model that was used in previous study of lanthanide opacities, i.e. the dynamical ejecta has a mass of 1.4×10^{-2} M$_\odot$ and mean ejecta speed of 0.125c (maximum speed of 0.25c). We present the bolometric luminosity for this model in Fig. 8. From this light-curve comparison, we observe that using U as a surrogate for the entire set of actinides overpredicts the peak of the luminosity by only 10–20% relative to the other two, more complete, actinide distributions. The latter two curves display even less discrepancy at the peak. Outside of the peak region, the three curves display almost no sensitivity to the choice of actinide distribution.

In Fig. 9, we present the corresponding spectra at 1, 3 , 5 and 7 days. Overall, we observe moderately higher (20–30%) emission in the optical peaks for the pure-U curve, consistent with the luminosity comparison given in the previous paragraph. This discrepancy provides some indication of the level of inaccuracy that can occur in spectral modeling when approximating the opacity of the entire set of actinides with that of only uranium. At early times (1 and 3 days), all three curves display similar spectral features, but at later times, there is some differentiation between the pure-U curve and the other two curves that are obtained from more realistic actinide distributions. In particular, the latter two curves display a few spectral features above 40,000 Å that do not appear in the pure-U curve. On a practical note, these features occur in the infrared range and therefore are difficult to observe with ground-based telescopes due to absorption by various molecules in the Earth's atmosphere.

In order to better understand the source of these far-IR features, we recalculated the spectrum presented in Fig. 9, using the limited-range distribution ($Z = 89–98$), but with each of the ten actinide elements removed from the calculation, one at a time. We found that a single actinide, Pa ($Z = 91$), is largely responsible for these long-wavelength features, as displayed in Fig. 10. The day-5 and day-7 panels in this figure clearly indicate the importance of Pa for these weak features above 40,000 Å. Furthermore, all four panels indicate that Pa has a moderate, but noticeable, effect on the strong infrared peaks below 40,000 Å. We defer a more detailed study of this effect to future work.

4.2 Emission study using a grid of ejecta masses and speeds

The appearance of those features above 40,000 Å provide motivation for a more in-depth search for spectral features that might be observable and that could be used to distinguish between the partial- and full-actinide distributions. So we next consider a grid of three ejecta masses (0.003, 0.01, 0.03 M$_\odot$) and three ejecta speeds (0.05c, 0.15c, 0.3c), which, when combined with the three actinide distributions, yields a total of 27 models to investigate. This 3x3 grid represents a subset of the simulation cube considered in our earlier work (Wollaeger et al. 2021), with the minimum and maximum masses omitted in order to focus on the most likely KN events.

In Fig. 11 we present the light curves for this 3x3 grid, with the ejecta mass held constant in each row and the density held constant in each column. As expected, the lowest velocity simulations (first column) produce broad light curves and the highest velocity simulations (third column) produce much narrower light curves. For any given pair of mass-velocity values, it is straightforward to see that the partial- and full-actinide distributions track each other very closely, with the latter producing slightly higher peak luminosity, while the pure-U curve produces the highest peak values and displays a qualitatively different behavior for the three cases with the lowest velocity.

The corresponding spectra for the 3x3 grid can be similarly organized, i.e. keeping the velocity fixed produces similar spectra. As a specific example, we present in Fig. 12 the spectra at 1, 3, 5 and 7 days for the case of 0.003 M$_\odot$ and 0.30c. From this figure, we again see that the partial- and full-actinide results are very similar, while the pure-U curve displays different behavior over most of the simulation time.

For the sake of brevity, we do not display the additional four-panel spectral figures for the remaining eight mass-velocity pairs. Instead, in order to analyze these results in a more convenient and efficient manner, we consider the L1 spectral norm, given by

$$\text{L1} = \int_{\lambda_{\min}}^{\lambda_{\max}} d\lambda \, |F_x(\lambda) - F_{\text{baseline}}(\lambda)| / \int_{\lambda_{\min}}^{\lambda_{\max}} d\lambda \, F_{\text{baseline}}(\lambda) ,$$

$$(3)$$

where $F_x(\lambda)$ is the flux computed with either the partial- or complete-actinide distribution, and the baseline reference, $F_{\text{baseline}}(\lambda)$, is chosen to be the flux computed with the pure-U distribution. For each of the two actinide distributions ($89 \leq Z \leq 98$ or $89 \leq Z \leq 102$), L1-norm curves are computed for the nine possible pairs of mass-velocity values described above, as a function of time.

We present comparisons of the L1 spectral norm in Fig. 13. Results are presented for the L1 norm computed over three wavelength ranges: the full wavelength range from $10^3–10^5$ Å (essentially the total spectrum), a more limited wavelength range from $10^4–10^5$ Å
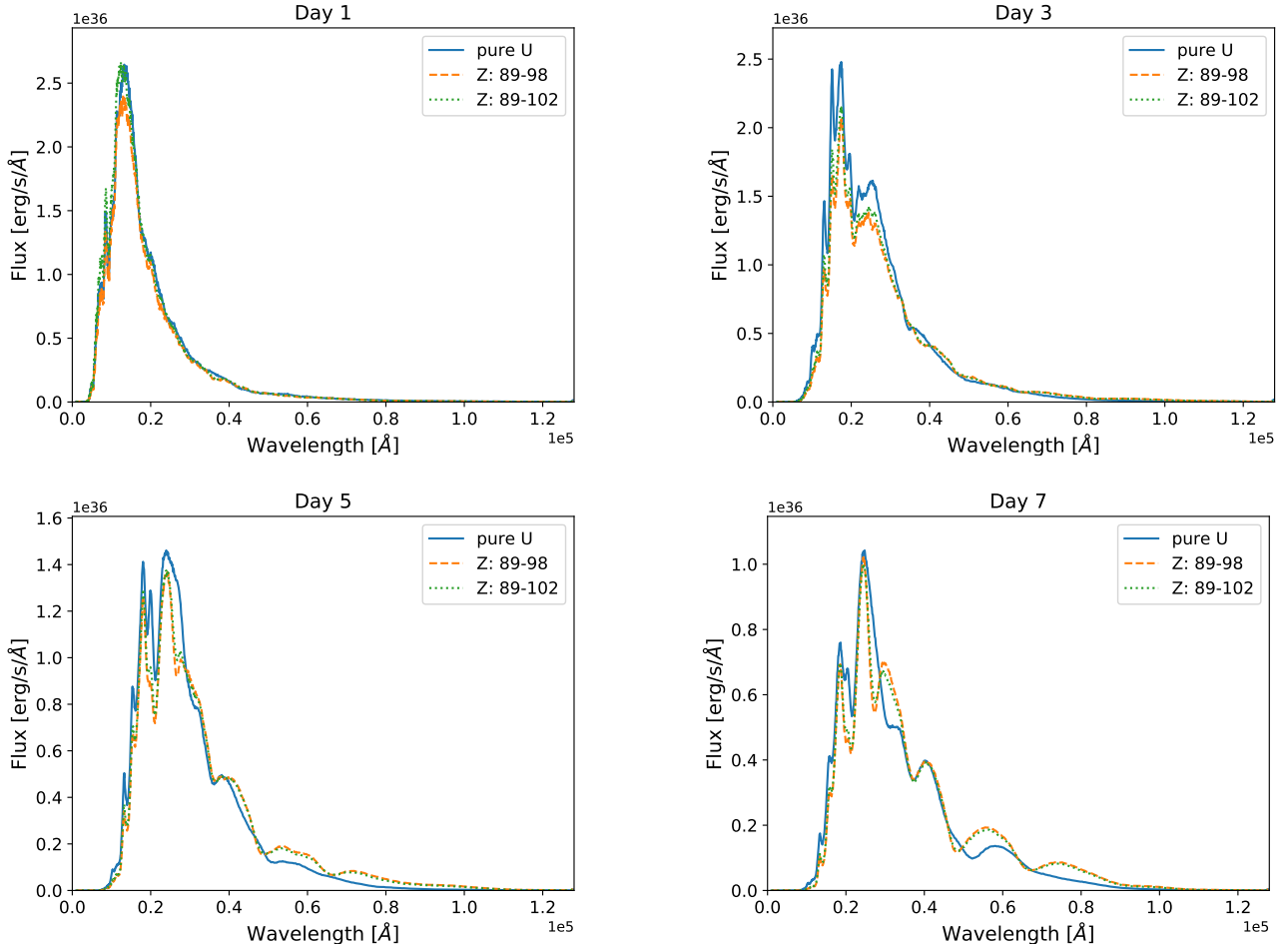
Figure 9. Spectra at 1, 3, 5 and 7 days for the first dynamical ejecta model, with a mass of 1.4×10^{-2} M$_\odot$ and mean ejecta speed of $0.125c$. Results are displayed for three different actinide abundance distributions: pure U (solid blue curve), a uniform distribution including only a limited range of actinides from $Z = 89$–98 (dashed orange curve), and a uniform distribution including the entire range of actinides from $Z = 89$–102 (green dotted curve).

(from near-IR to longer wavelengths) and an even more limited wavelength range from 4×10^4–10^5 Å (from mid-IR to longer wavelengths). In each panel, the solid curves represent the L1 norm computed for the partial-actinide distribution and the dashed curves represent the L1 norm computed for the complete-actinide distribution. Thus, each panel contains nine solid curves and nine dashed curves, corresponding to the nine possible pairs of mass and speed values described above.

Before offering some analysis of these results, we first provide a brief explanation of the rich amount of information that can be displayed in these time-dependent curves. There are three particular items of interest for this study: (1) Choosing the pure-U result as the baseline flux is useful in an absolute sense because (for a fixed mass-velocity pair) a given L1 curve displays the inaccuracy that occurs due to choosing only uranium as a surrogate for a more complete set of actinides. (2) On the other hand, for relative L1-norm comparisons, the choice of baseline flux is not too important. More specifically, for a fixed mass-velocity pair, significant differences that occur when comparing the two L1 curves resulting from each actinide distribution indicate the existence of spectral features that could be used to distinguish between the two abundance patterns. (3) Alternatively, for a fixed actinide distribution, differences that occur when comparing curves produced with different mass-velocity pairs indi-

cate possible spectral features of general interest due to the presence of actinide elements.

Returning to Fig. 13, and keeping in mind the above three items of interest, we note the following patterns: (1) the maximum value for each solid or dashed curve occurs between about 1–20 days, depending on the particular mass-velocity pair, and the maximum value is approximately one, which indicates a difference of a factor of approximately two in the integrated flux. (2) For a fixed mass-velocity pair, the two abundance curves agree reasonably well, indicating that there is not much spectral sensitivity to the two actinide distributions considered here. (3) For either actinide distribution, the various mass-velocity curves display very similar behavior when considering fixed mass or fixed velocity, provided that the curves are appropriately shifted forward or backward in time. The lack of abrupt changes in the maximum L1-norm values (provided that the time-shift effect is taken into account; see more details below) indicates that different spectral features are not appearing and disappearing as a function of different mass-velocity conditions.

Returning to the time-shift behavior, we note that this pattern is expected from basic physics considerations of a homologous expansion, i.e. increasing the ejecta velocity makes line expression occur sooner in time, while increasing the ejecta mass (or density) produces a slower evolution of the expansion and the spectral features
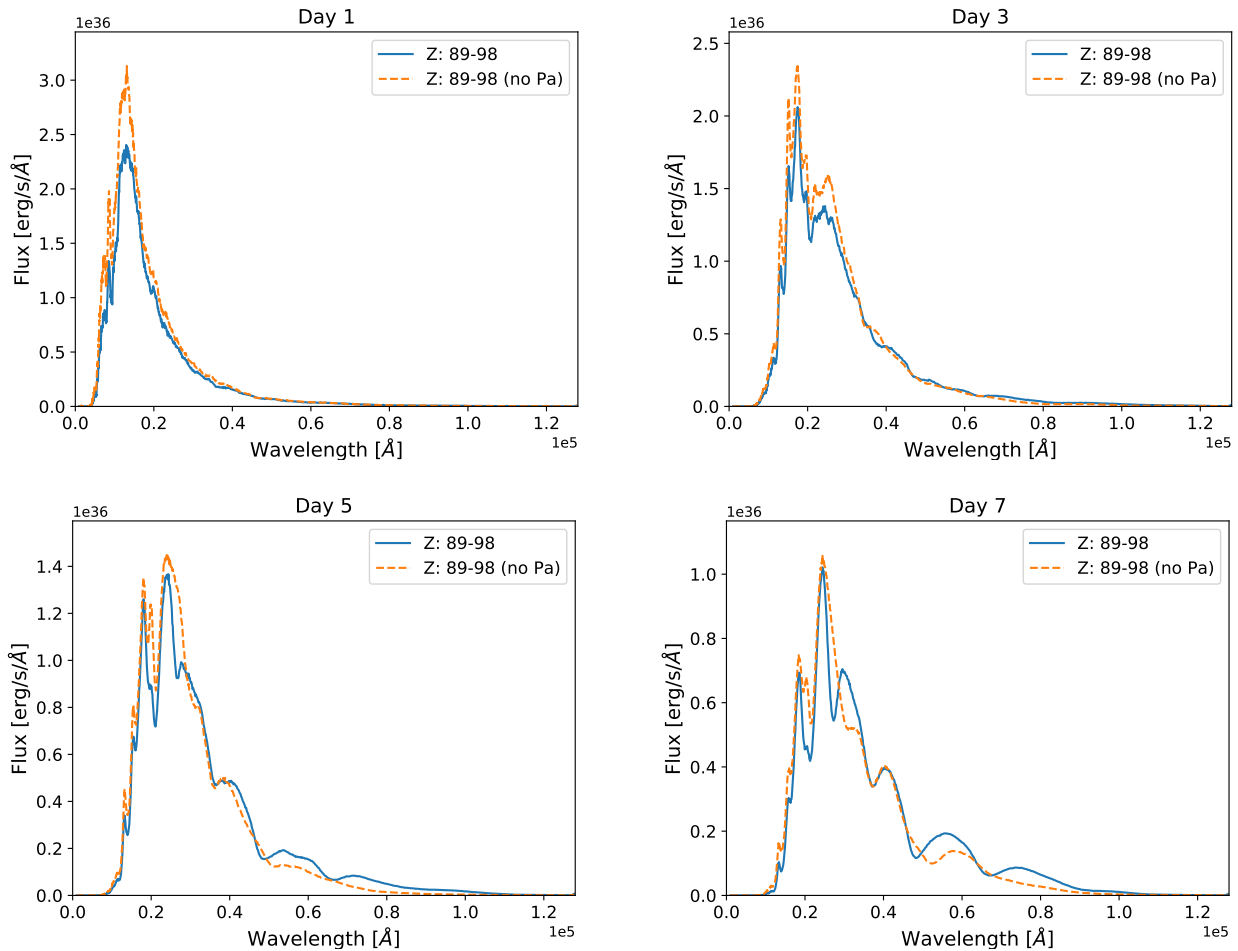
Figure 10. Spectra at 1, 3, 5 and 7 days for the first dynamical ejecta model, with a mass of 1.4×10^{-2} M$_\odot$ and mean ejecta speed of $0.125c$. Results are displayed for two different actinide abundance distributions: a limited range of actinides from $Z = 89$–98 (solid blue curve) and the same limited range of actinides, but with Pa ($Z = 91$) removed from the calculation (dashed orange curve).

evolve on a longer time scale. More specifically, the trends in the L1 norm are expected when considering the evolution of the photosphere. The optical depth of the ejecta scales as $L \times \rho \times \kappa$, where L is the sizescale of the ejecta, ρ is the density and κ is the opacity. Assuming that the expansion dominates the sizescale, the optical depth scales as $M_{\mathrm{ejecta}}\,\kappa/v_{\mathrm{ejecta}}^2$. The variations in the models in Fig. 13 roughly follow these trends. Arnett derived a more detailed picture for Type Ia supernovae (Arnett 1979, 1982), where the shape function of the emission could be reduced by a similar parameter $y = (M_{\mathrm{ejecta}}\,\kappa/v_{\mathrm{ejecta}})^{1/2}$. Although we do not provide a full comparison with the Arnett derivation here, we note that the trends in our KN simulations are close to those predicted with that analytic model.

In order to illustrate these trends, we present in Fig. 14 a comparison of three spectra for which the mean ejecta speed is fixed at the middle grid value of $0.15c$ and the ejecta mass takes on each of the three grid values (0.003, 0.01, 0.03 M$_\odot$). These spectra are generated with the partial-actinide distribution, but the results are expected to be the same for the complete-actinide distribution. The three spectra are plotted at the times that correspond to their maximum L1-norm values in the lower right-hand panel of Fig. 13, i.e. day 6.9, 9.6 and 13.4, respectively. Note that the various spectral features in each curve align almost perfectly in their wavelength po-

sitions when the time shift is applied. When applying the same type of time-shift analysis to the opposite situation, in which the ejecta mass is held fixed while the mean speed is allowed to change, we find that the spectral features also become better aligned, although the agreement in relative feature strength is not as good as that displayed in Fig. 13. We attribute this poorer agreement to the fact that Doppler broadening, which is important in determining the shapes of the spectral features, depends strongly on the ejecta velocity. Thus, taking into account the time-shift analysis and the above three items of interest, a main conclusion of this work is that ejecta mass and velocity play a more significant role in modeling KN emission than the choice of actinide abundances. Furthermore, specific mass-velocity conditions shift the line emission earlier or later in time, but do not result in the production of spectral features that arise from different atomic transitions.

5 SUMMARY

We have made a first attempt to calculate a complete set of actinide opacities for use in KN modeling. Basic trends observed in the actinide opacities follow similar patterns that were observed previously for lanthanide opacities, e.g. a dominant contribution from line
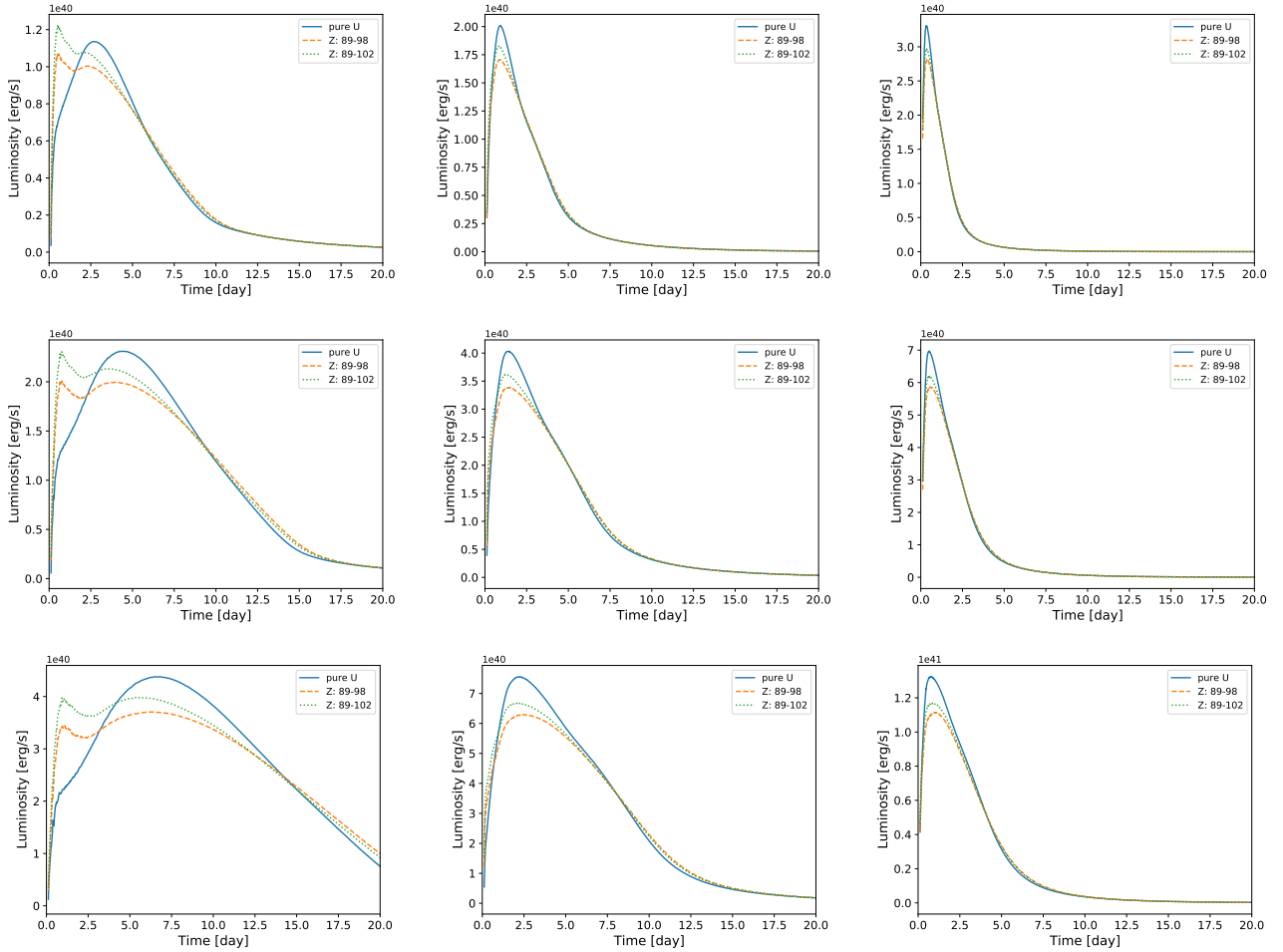
Figure 11. Bolometric luminosity for the 3x3 grid of masses and velocities considered in this work. The mass is constant in each row, while the velocity is constant in each column. Results for the lowest mass-velocity pair (0.003 M$_\odot$, 0.05c) are displayed in the upper left-hand corner and for the highest mass-velocity pair (0.03 M$_\odot$, 0.3c), in the lower right-hand corner. Results are displayed for three different actinide abundance distributions: pure U (solid blue curve), a uniform distribution including only a limited range of actinides from $Z = 89$–98 (dashed orange curve), and a uniform distribution including the entire range of actinides from $Z = 89$–102 (green dotted curve).

absorption over a significant fraction of the wavelength range that is relevant for KN emission. The bound-bound contribution to these opacities was computed with a line-binned approach, which allows for the generation of tabulated opacities, independent of the particular type of hydrodynamic expansion that is chosen. These tabular opacities will be made available on NIST-LANL opacity website (Olsen et al. 2020), concurrent with the publication of this article, to aid in KN modeling efforts.

These actinide opacities were used in simulations of KN light curves and spectra in order to explore the sensitivity to different actinide abundance distributions predicted by nuclear theory. The simulations were carried out for a range of ejecta masses and speeds, while the nuclear heating rate was held fixed. We found a relative lack of importance of the heavier actinides on KN emission, making it difficult to distinguish between the two abundance distributions considered in this study. This behavior is consistent with the corresponding lack of importance of the heavier lanthanide elements observed in previous studies. This behavior is a consequence of the energy-level spacing of low-lying levels and the resulting positions of absorption line features. For the lighter actinides, our modeling indicates that protactinium is responsible for the production of faint,

mid-IR features above 40,000 Å at 5–7 days post merger, and also has a very moderate effect on the strong (near-IR) features that occur around the peak of the emission at 1–7 days post merger. Compared to variation in actinide abundances, we found that the choice of ejecta mass and velocity has a more significant effect on the behavior of KN emission. Future work is planned to study various sensitivities to actinide elements in more detail.
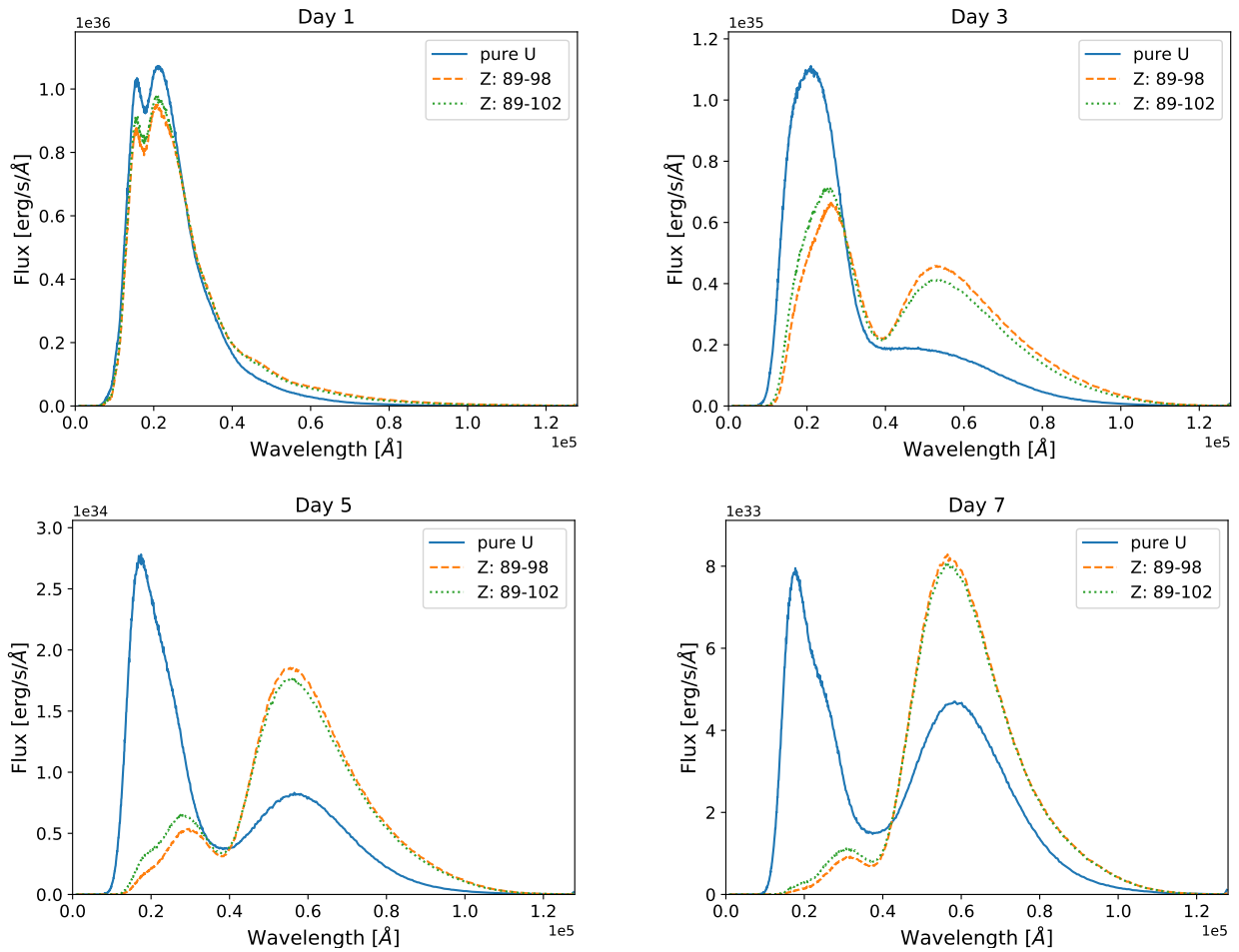
Figure 12. Spectra at 1, 3, 5 and 7 days for an ejecta mass of 0.003 $M_\odot$ and mean ejecta speed of $0.3c$. Results are displayed for three different actinide abundance distributions: pure U (solid blue curve), a uniform distribution including only a limited range of actinides from $Z = 89$–98 (dashed orange curve), and a uniform distribution including the entire range of actinides from $Z = 89$–102 (green dotted curve).

DATA AVAILABILITY

The opacities described in this work will be made available at the NIST-LANL opacity website: https://nlte.nist.gov/OPAC.
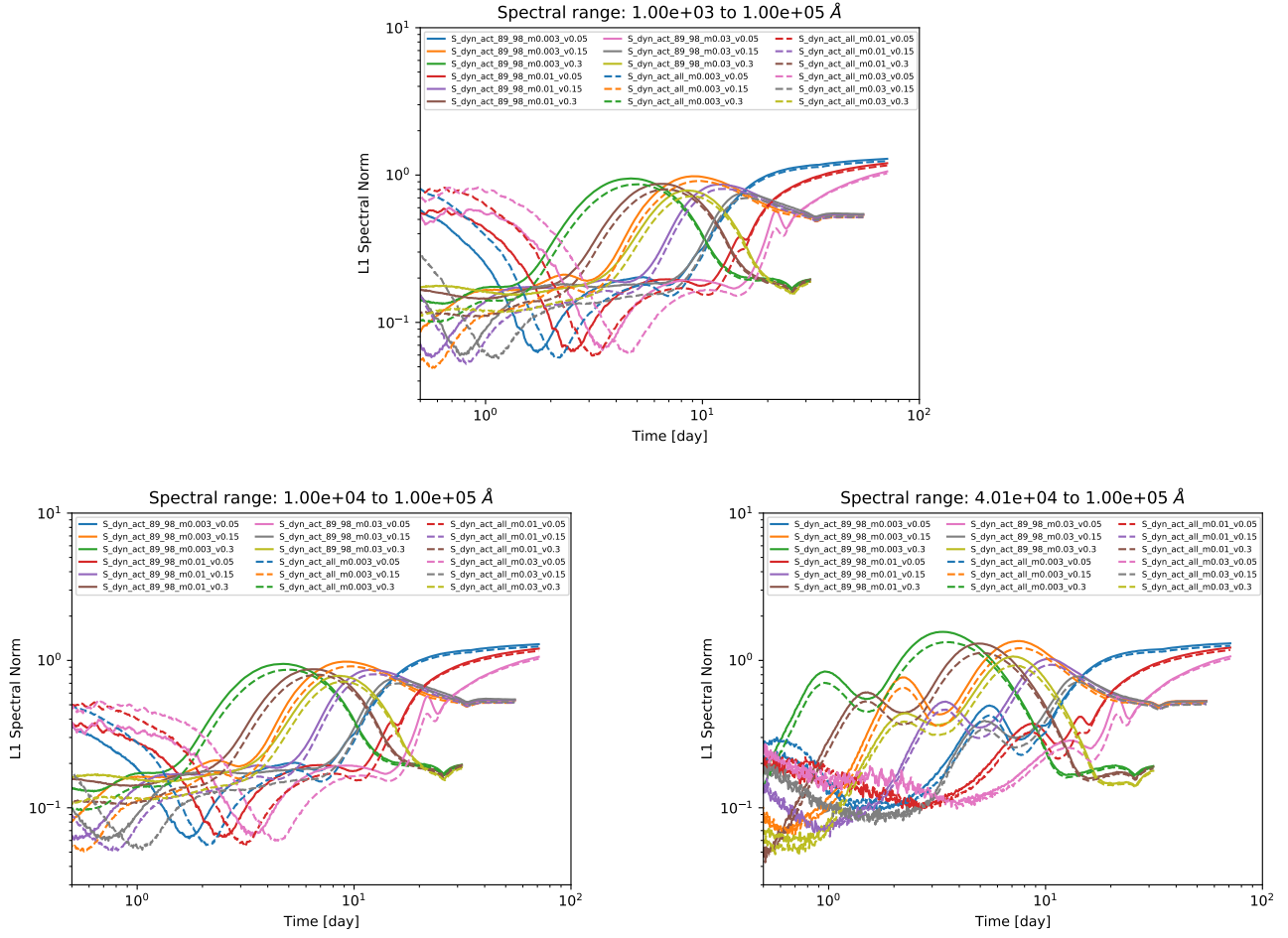
Figure 13. L1 spectral norm as a function of time, computed over three wavelength ranges: the full wavelength range from 10^3–10^5 Å (upper panel), a more limited wavelength range from 10^4–10^5 Å (bottom left-hand panel) and an even more limited wavelength range from 4×10^4–10^5 Å (bottom right-hand panel). The L1 norm is calculated according to equation (3), with the pure-U spectrum chosen to be the baseline. In each panel, the nine solid curves represent the L1 norm for the partial-actinide distribution and the nine dashed curves represent the L1 norm for the complete-actinide distribution. The nine curves correspond to different pairs of ejecta mass and speed (see text for details).
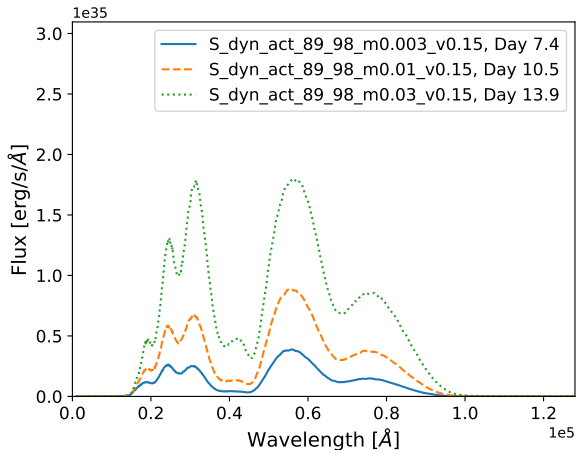
Figure 14. Spectra for three different mass-velocity pairs: the mean ejecta speed is fixed at $0.15c$ and the ejecta masses are 0.003, 0.01, 0.03 M$_\odot$, represented by solid blue, dashed orange, and dotted blue curves, respectively. The spectra are calculated at different times, corresponding to the peak L1-norm values displayed in the lower right-hand panel of Fig. 13, i.e. at 6.9, 9.6 and 13.4 days, respectively. These spectra are all generated with the limited range of actinide abundances ($Z = 89$–98).

REFERENCES

Abbott B. P., et al., 2017a, Physical Review Letters, 119, 161101
Abbott B. P., et al., 2017b, ApJ, 848, L12
Abdallah J., R.E.H. Clark R.D. Cowan 1988, Los Alamos Manual LA-11436-M, Vol. I
Arnett W. D., 1979, ApJ, 230, L37
Arnett W. D., 1982, ApJ, 253, 785
Audi G., Kondev F. G., Wang M., Huang W. J., Naimi S., 2017, Chinese Physics C, 41, 030001
Banerjee S., Tanaka M., Kawaguchi K., Kato D., Gaigalas G., 2020, ApJ, 901, 29
Barnes J., Kasen D., 2013, ApJ, 775, 18
Bulla M., et al., 2021, MNRAS, 501, 1891
Carvajal Gallego H., Berengut J. C., Palmeri P., Quinet P., 2021, Monthly Notices of the Royal Astronomical Society, 509, 6138
Carvajal Gallego H., Berengut J. C., Palmeri P., Quinet P., 2022, Monthly Notices of the Royal Astronomical Society, 513, 2302
Castor J. L., 1974, MNRAS, 169, 279
Chase E. A., et al., 2021, arXiv e-prints, p. arXiv:2105.12268
Colgan J., et al., 2016, ApJ, 817, 116
Côté B., et al., 2017, ApJ,
Côté B., et al., 2021, Science, 371, 945
Cowan R. D., 1981, The theory of atomic structure and spectra. Berkeley: University of California Press
Domoto N., Tanaka M., Wanajo S., Kawaguchi K., 2021, ApJ, 913, 26
Even W., et al., 2020, ApJ, 899, 24
Fontes C. J., Fryer C. L., Hungerford A. L., Hakel P., Colgan J., Kilcrease D. P., Sherrill M. E., 2015a, High Energy Density Physics, 16, 53
Fontes C. J., et al., 2015b, Journal of Physics B Atomic Molecular Physics, 48, 144014
Fontes C. J., Colgan J., Abdallah Jr J., 2016, in Ralchenko Y., ed., , Modern Methods in Collisional-Radiative Modeling of Plasmas. New York: Springer, p. 17
Fontes C. J., Fryer C. L., Hungerford A. L., Wollaeger R. T., Rosswog S., Berger E., 2017, preprint, (arXiv:1702.02990)
Fontes C. J., Fryer C. L., Hungerford A. L., Wollaeger R. T., Korobkin O., 2020, MNRAS, 493, 4143
Frey L. H., Even W., Whalen D. J., Fryer C. L., Hungerford A. L., Fontes C. J., Colgan J., 2013, ApJS, 204, 16
Gaigalas G., Kato D., Rynkun P., Radžiūtė L., Tanaka M., 2019, ApJS, 240, 29
Gillanders J. H., McCann M., Sim S. A., Smartt S. J., Ballance C. P., 2021, MNRAS, 506, 3560
Goriely S., Samyn M., Pearson J. M., 2007, Phys. Rev. C, 75, 064312
Goriely S., Chamel N., Pearson J. M., 2009, Phys. Rev. Lett., 102, 152503
Grant I. P., 2007, Relativistic quantum theory of atoms and molecules: theory and computation. Springer
Hakel P., Kilcrease D. P., 2004, in Cohen J. S., Kilcrease D. P., Mazevet S., eds, American Institute of Physics Conference Series Vol. 730, American Institute of Physics Conference Series. p. 190, doi:10.1063/1.1824870
Hakel P., et al., 2006, J. Quant. Spectrosc. Radiative Transfer, 99, 265
Holmbeck E. M., Sprouse T. M., Mumpower M. R., Vassh N., Surman R., Beers T. C., Kawano T., 2019a, ApJ, 870, 23
Holmbeck E. M., Frebel A., McLaughlin G. C., Mumpower M. R., Sprouse T. M., Surman R., 2019b, ApJ, 881, 5
Horowitz C. J., et al., 2019, Journal of Physics G Nuclear Physics, 46, 083001
Hotokezaka K., Tanaka M., Kato D., Gaigalas G., 2021, MNRAS, 506, 5863
Huebner W. F., Barfield W. D., 2014, Opacity. Astrophysics and Space Science Library Vol. 402, New York: Springer, doi:10.1007/978-1-4614-8797-5
Karp A. H., Lasher G., Chan K. L., Salpeter E. E., 1977, ApJ, 214, 161
Kasen D., Badnell N. R., Barnes J., 2013, ApJ, 774, 25
Kasen D., Fernández R., Metzger B. D., 2015, MNRAS, 450, 1777
Kasen D., Metzger B., Barnes J., Quataert E., Ramirez-Ruiz E., 2017, Nature, 551, 80
Kawaguchi K., Shibata M., Tanaka M., 2018, ApJ, 865, L21
Kawaguchi K., Shibata M., Tanaka M., 2020, ApJ, 889, 171

Kawaguchi K., Fujibayashi S., Shibata M., Tanaka M., Wanajo S., 2021, ApJ, 913, 100
Kawano T., Capote R., Hilaire S., Chau Huu-Tai P., 2016, Physical Review C, 94
Korobkin O., Rosswog S., Arcones A., Winteler C., 2012, MNRAS, 426, 1940
Korobkin O., et al., 2020, ApJ, 889, 168
Korobkin O., et al., 2021, ApJ, 910, 116
Kortelainen M., McDonnell J., Nazarewicz W., Reinhard P. G., Sarich J., Schunck N., Stoitsov M. V., Wild S. M., 2012, Phys. Rev. C, 85, 024304
Koura H., 2014, Progress of Theoretical and Experimental Physics, 2014, 113D02
Koura H., Tachibana T., Uno M., Yamada M., 2005, Progress of Theoretical Physics, 113, 305
Kramida A., Ralchenko Yu., Reader J., and NIST ASD Team 2018, NIST Atomic Spectra Database (ver. 5.6.1), [Online]. Available: https://physics.nist.gov/asd [2019, January 29]. National Institute of Standards and Technology, Gaithersburg, MD.
Kulkarni S. R., 2005, ArXiv Astrophysics e-prints,
Li L.-X., Paczyński B., 1998, ApJ, 507, L59
Magee N. H., et al., 2004, in Cohen J. S., Kilcrease D. P., Mazevet S., eds, American Institute of Physics Conference Series Vol. 730, American Institute of Physics Conference Series. New York: AIP, p. 168, doi:10.1063/1.1824868
Metzger B. D., et al., 2010, MNRAS, 406, 2650
Möller P., Sierk A. J., Ichikawa T., Iwamoto A., Mumpower M., 2015, Phys. Rev. C, 91, 024310
Möller P., Sierk A. J., Ichikawa T., Sagawa H., 2016, Atomic Data and Nuclear Data Tables, 109, 1
Möller P., Mumpower M. R., Kawano T., Myers W. D., 2019, Atomic Data and Nuclear Data Tables, 125, 1
Mumpower M., Surman R., Fang D.-L., Beard M., Möller P., Kawano T., Aprahamian A., 2015, Physical Review C, 92, 035807
Mumpower M. R., Surman R., McLaughlin G. C., Aprahamian A., 2016a, Progress in Particle and Nuclear Physics, 86, 86
Mumpower M. R., Surman R., McLaughlin G. C., Aprahamian A., 2016b, Progress in Particle and Nuclear Physics, 86, 86
Mumpower M. R., Kawano T., Möller P., 2016c, Phys. Rev. C, 94, 064317
Mumpower M. R., Kawano T., Ullmann J. L., Krtička M., Sprouse T. M., 2017, Phys. Rev. C, 96, 024612
Mumpower M. R., Kawano T., Sprouse T. M., Vassh N., Holmbeck E. M., Surman R., Möller P., 2018, ApJ, 869, 14
O'Connor B., et al., 2021, MNRAS, 502, 1279
Olsen K., Fontes C. J., Fryer C. L., Hungerford A. L., Wollaeger R. T., Korobkin O., 2020, NIST-LANL Opacity Database (ver. 1.0), [Online]. Available: [Online]. Available: https://nlte.nist.gov/OPAC. National Institute of Standards and Technology, Gaithersburg, MD.
Piran T., Nakar E., Rosswog S., 2013, MNRAS, 430, 2121
Quinet P., Palmeri P., 2020, Atoms, 8
Radžiūtė L., Gaigalas G., Kato D., Rynkun P., Tanaka M., 2020, ApJS, 248, 17
Ristic M., et al., 2021, arXiv e-prints, p. arXiv:2105.07013
Rose S. J., Grant I. P., Pyper N. C., 1978, Journal of Physics B Atomic Molecular Physics, 11, 1171
Rosswog S., Piran T., Nakar E., 2013, Monthly Notices of the Royal Astronomical Society, 430, 2585
Sobolev V. V., 1960, Moving envelopes of stars. Cambridge: Harvard University Press
Sprouse T. M., Navarro Perez R., Surman R., Mumpower M. R., McLaughlin G. C., Schunck N., 2020, Phys. Rev. C, 101, 055803
Sprouse T. M., Mumpower M. R., Surman R., 2021, Phys. Rev. C, 104, 015803
Tanaka M., Hotokezaka K., 2013, ApJ, 775, 113
Tanaka M., et al., 2018, ApJ, 852, 109
Tanaka M., Kato D., Gaigalas G., Kawaguchi K., 2020, MNRAS, 496, 1369
Tanvir N. R., et al., 2017, ApJ, 848, L27
Tatewaki H., Yamamoto S., Hatano Y., 2017, ACS Omega, 2, 6072
Troja E., et al., 2017, Nature, 551, 71

Vassh N., et al., 2019, Journal of Physics G Nuclear Physics, 46, 065202

Vassh N., Mumpower M. R., McLaughlin G. C., Sprouse T. M., Surman R., 2020, ApJ, 896, 28

Viola Jr V. E., Seaborg G. T., 1966, Journal of Inorganic and Nuclear Chemistry (England) Merged with Inorg. Nucl. Chem. Lett. to form Polyhedron, 28

Wanajo S., Sekiguchi Y., Nishimura N., Kiuchi K., Kyutoku K., Shibata M., 2014, ApJ, 789, L39

Wang M., Audi G., Kondev F. G., Huang W. J., Naimi S., Xu X., 2017, Chinese Physics C, 41, 030003

Wang X., et al., 2020, ApJ, 903, L3

Watson D., et al., 2019, Nature, 574, 497

Wollaeger R. T., van Rossum D. R., 2014, ApJS, 214, 28

Wollaeger R. T., et al., 2018, MNRAS, 478, 3298

Wollaeger R. T., et al., 2019, ApJ, 880, 22

Wollaeger R. T., et al., 2021, ApJ, 918, 10

Wu M.-R., Barnes J., Martínez-Pinedo G., Metzger B. D., 2019, Phys. Rev. Lett., 122, 062701

Zhu Y., et al., 2018, ApJ, 863, L23

Zhu Y. L., Lund K. A., Barnes J., Sprouse T. M., Vassh N., McLaughlin G. C., Mumpower M. R., Surman R., 2021, ApJ, 906, 94

APPENDIX A: LIST OF CONFIGURATIONS USED IN THIS WORK

Table A1 in this appendix contains a list of configurations that were used in calculating the energy levels and oscillator strengths for the 14 actinide elements considered in this work. Based on the relevant conditions of kilonova ejecta, only the first four ion stages were calculated for each element. The list of configurations was chosen to obtain a good representation of the lowest lying energy levels that are necessary to: (a) obtain converged atomic level populations via Saha-Boltzmann statistics and (b) calculate converged opacities with respect to the number of bound-bound transitions in the photon energy range of interest. The choice of configurations was based on the energy-level entries in the NIST database (Kramida et al. 2018), when available, as well as ab initio atomic structure calculations.

This paper has been typeset from a TEX/LATEX file prepared by the author.

Table A1. A list of configurations, number of fine-structure levels, and number of (electric dipole) absorption lines for the various ion stages considered in this work. A completely filled Rn core is assumed for the 14 actinide elements. For the first two ion stages of nobelium, No I and II, the orbital angular momentum symbol ℓ represents the range of values $\ell = s, p, d, f$ and g.

Ion stage	Configurations	# of levels	# of lines
Ac I	$6d^17s^2, 6d^27s^1, 7s^27p^1, 6d^17s^17p^1, 6d^27p^1,$ $6d^3, 5f^17s^2, 5f^16d^17s^1, 5f^17s^17p^1, 5f^16d^2, 5f^16d^17p^1$	366	16,164
Ac II	$7s^2, 6d^17s1, 6d^2, 7s^17p^1, 6d^17p^1,$ $5f^17s^1, 5f^16d^1, 7s^18s^1, 5f^17p^1, 5f^2$	81	797
Ac III	$7s^1, 6d^1, 5f^1, 7p^1$	7	8
Ac IV	$6p^6, 6p^57s^1, 6p^56d^1, 6p^55f^1, 6p^57p^1$	39	211
Th I	$6d^27s^2, 6d^37s^1, 5f^16d^17s^2, 6d^17s^27p^1, 6d^27s^17p^1, 5f^16d^27s^1,$ $5f^17s^27p^1, 6d^4, 5f^16d^17s^17p^1, 5f^27s^2, 5f^17s^27p^1, 5f^16d^3,$ $6d^37p^1, 5f^16d^27p^1, 5f^27s^17p^1, 5f^26d^2, 5f^26d^17s^1, 5f^26d^17p^1$	2851	802,472
Th II	$6d^17s^2, 6d^27s^1, 5f^17s^2, 5f^16d^17s^1, 6d^3, 5f^16d^2, 6d^17s^17p^1,$ $5f^27s^1, 5f^17s^17p^1, 5f^16d^17p^1, 7s^27p^1, 5f^26d^1, 6d^27p^1, 5f^27p^1$	566	35,724
Th III	$5f^16d^1, 6d^2, 5f^17s^1, 6d^17s^1, 5f^2, 5f^17p^1, 6d^17p^1, 7s^17p^1$	78	759
Th IV	$5f^1, 7s^1, 6d^1, 7p^1$	7	8
Pa I	$5f^37s^2, 5f^26d^17s^2, 5f^26d^27s^1, 5f^36d^17s^1, 5f^36d^2, 5f^26d^17s^17p^1,$ $5f^36d^17p^1, 5f^37s^17p^1, 5f^16d^27s^2, 5f^16d^27s^17p^1, 5f^26d^27p^1$	10,985	10,501,071
Pa II	$5f^27s^2, 5f^37s^1, 5f^36d^1, 5f^37p^1, 5f^26d^2, 5f^26d^17s^1, 5f^26d^17p^1,$ $5f^27s^17p^1, 5f^16d^27s^1, 5f^16d^27p^1, 6d^37s^1, 6d^37p^1$	2,940	816,301
Pa III	$5f^3, 5f^27s^1, 5f^26d^1,$ $5f^27p^1, 5f^16d^2, 5f^16d^17s^1$	361	12,394
Pa IV	$5f^2, 5f^17s^1, 5f^16d^1, 5f^17p^1, 6d^2, 6d^17s^1$	62	452
U I	$5f^47s^2, 5f^36d^17s^2, 5f^46d^17s^1,$ $5f^46d^2, 5f^36d^17s^17p^1, 5f^46d^17p^1$	16,882	20,948,831
U II	$5f^37s^2, 5f^47s^1, 5f^46d^1, 5f^47p^1,$ $5f^36d^2, 5f^36d^17s^1, 5f^36d^17p^1, 5f^37s^17p^1$	6,929	4,016,742
U III	$5f^4, 5f^37s^1, 5f^36d^1, 5f^37p^1,$ $5f^26d^2, 5f^26d^17s^1, 5f^16d^27s^1$	1,650	233,822
U IV	$5f^3, 5f^27s^1, 5f^26d^1, 5f^27p^1$	241	5,784
Np I	$5f^57s^2, 5f^46d^17s^2, 5f^56d^17s^1, 5f^56d^2,$ $5f^46d^17s^17p^1, 5f^56d^17p^1, 5f^57s^17p^1$	37,504	102,137,419
Np II	$5f^57s^1, 5f^56d^1, 5f^57p^1, 5f^46d^2,$ $5f^46d^17s^1, 5f^46d^17p^1, 5f^47s^17p^1$	16,595	21,306,572
Np III	$5f^5, 5f^47s^1, 5f^46d^1, 5f^47p^1,$ $5f^36d^2, 5f^36d^17s^1, 5f^26d^27s^1$	5,274	2,262,369
Np IV	$5f^4, 5f^37s^1, 5f^36d^1, 5f^37p^1$	817	57,765
Pu I	$5f^67s^2, 5f^56d^17s^2, 5f^66d^17s^1, 5f^66d^2,$ $5f^56d^17s^17p^1, 5f^66d^17p^1, 5f^67s^17p^1, 5f^67p^2$	65,015	276,327,167
Pu II	$5f^67s^1, 5f^66d^1, 5f^67p^1, 5f^56d^2,$ $5f^56d^17s^1, 5f^56d^17p^1, 5f^57s^17p^1, 5f^57p^2$	32,828	82,524,211
Pu III	$5f^6, 5f^57s^1, 5f^56d^1, 5f^57p^1,$ $5f^46d^2, 5f^46d^17s^1, 5f^36d^27s^1, 5f^47s^2$	13,277	13,511,494
Pu IV	$5f^5, 5f^47s^1, 5f^46d^1, 5f^47p^1$	1,994	320,633
Am I	$5f^77s^2, 5f^66d^17s^2, 5f^76d^17s^1, 5f^76d^2, 5f^66d^27s^1, 5f^66d^17s^17p^1, 5f^76d^17p^1,$ $5f^77s^17p^1, 5f^77s^17d^1, 5f^77s^18s^1, 5f^77s^18p^1, 5f^76d^17d^1, 5f^76d^18s^1, 5f^76d^18p^1$	164,455	1,939,681,964
Am II	$5f^77s^1, 5f^76d^1, 5f^77p^1, 5f^66d^2, 5f^66d^17s^1,$ $5f^66d^17p^1, 5f^67s^17p^1, 5f^77d^1, 5f^78s^1$	46,213	152,795,857
Am III	$5f^7, 5f^67s^1, 5f^66d^1,$ $5f^67p^1, 5f^56d^2, 5f^56d^17s^1$	17,058	13,844,004
Am IV	$5f^6, 5f^57s^1, 5f^56d^1, 5f^57p^1$	3,737	1,045,697
Cm I	$5f^87s^2, 5f^76d^17s^2, 5f^76d^27s^1, 5f^76d^27p^1, 5f^77s^27p^1,$ $5f^77s^17p^2, 5f^76d^3, 5f^86d^17s^1, 5f^86d^2, 5f^76d^17s^17p^1,$ $5f^86d^17p^1, 5f^87s^17p^1, 5f^97s^1, 5f^96d^1, 5f^97p^1$	231,490	3,707,210,225
Cm II	$5f^87s^1, 5f^86d^1, 5f^87p^1, 5f^76d^2, 5f^77s^2, 5f^76d^17s^1, 5f^76d^17p^1,$ $5f^77s^17p^1, 5f^66d^17s^2, 5f^66d^27s^1, 5f^77s^17d^1, 5f^77s^18s^1, 5f^77s^18p^1,$ $5f^76d^17d^1, 5f^76d^18s^1, 5f^76d^18p^1, 5f^9, 5f^87d^1, 5f^88s^1, 5f^88p^1$	142,841	1,490,279,275
Cm III	$5f^8, 5f^77s^1, 5f^76d^1,$ $5f^77p^1, 5f^66d^2, 5f^66d^17s^1$	23,268	21,734,676
Cm IV	$5f^7, 5f^67s^1, 5f^66d^1, 5f^67p^1$	5,323	2,073,702

Table A1. Continued…

Ion stage	Configurations	# of levels	# of lines
Bk I	$5f^97s^2$, $5f^86d^17s^2$, $5f^86d^27s^1$, $5f^87s^27p^1$, $5f^96d^17s^1$, $5f^96d^2$, $5f^86d^17s^17p^1$, $5f^96d^17p^1$, $5f^97s^17p^1$, $5f^97p^2$, $5f^96d^17d^1$, $5f^96d^18s^1$, $5f^96d^18p^1$, $5f^97s^17d^1$, $5f^97s^18s^1$, $5f^97s^18p^1$, $5f^{10}6d^1$, $5f^{10}7s^1$, $5f^{10}7p^1$, $5f^{10}7d^1$, $5f^{10}8s^1$, $5f^{10}8p^1$	130,293	1,240,175,537
Bk II	$5f^97s^1$, $5f^96d^1$, $5f^97p^1$, $5f^87s^2$, $5f^86d^2$, $5f^86d^17s^1$, $5f^86d^17p^1$, $5f^87s^17p^1$, $5f^97d^1$, $5f^98s^1$, $5f^98p^1$, $5f^{10}$	44,051	142,449,866
Bk III	$5f^9$, $5f^87s^1$, $5f^86d^1$, $5f^87p^1$, $5f^76d^2$, $5f^76d^17s^1$, $5f^77s^2$	24,992	21,470,795
Bk IV	$5f^8$, $5f^77s^1$, $5f^76d^1$, $5f^77p^1$	5,983	2,545,975
Cf I	$5f^{10}7s^2$, $5f^96d^17s2$, $5f^96d^17s17p1$, $5f^{10}6d^17s1$, $5f^{10}7s^17p1$, $5f^{10}7s^17d1$, $5f^{10}7s^18s^1$, $5f^{10}7s^18p^1$, $5f^97s^27p^1$, $5f^96d^27s^1$, $5f^{10}7p^2$, $5f^{10}6d^2$, $5f^{10}6d^17p^1$, $5f^{10}6d^17d^1$, $5f^{10}6d^18s^1$, $5f^{10}6d^18p^1$, $5f^96d^27p^1$	123,715	876,487,942
Cf II	$5f^{10}7s^1$, $5f^{10}6d^1$, $5f^{10}7p^1$, $5f^96d^2$, $5f^97s^2$, $5f^96d^17s^1$, $5f^96d^17p^1$, $5f^97s^17p^1$, $5f^{10}7d^1$, $5f^{10}8s^1$, $5f^{10}8p^1$, $5f^{11}$	28,805	63,361,823
Cf III	$5f^{10}$, $5f^97s^1$, $5f^96d^1$, $5f^97p^1$, $5f^86d^2$, $5f^86d^17s^1$, $5f^87s^2$	21,129	12,894,033
Cf IV	$5f^9$, $5f^87s^1$, $5f^86d^1$, $5f^87p^1$	5,194	1,943,961
Es I	$5f^{11}7s^2$, $5f^{10}6d^17s^2$, $5f^{10}6d^17s^17p^1$, $5f^{11}6d^17s^1$, $5f^{11}7s^17p^1$, $5f^{11}7s^17d^1$, $5f^{11}7s^18s^1$, $5f^{11}7s^18p^1$, $5f^{10}7s^27p^1$, $5f^{10}6d^27s^1$, $5f^{11}7p^2$, $5f^{11}6d^17p^1$, $5f^{11}6d^17d^1$, $5f^{11}6d^18s^1$, $5f^{11}6d^18p^1$, $5f^{10}6d^27p^1$, $5f^{11}6d^2$, $5f^{12}7s^1$, $5f^{12}6d^1$, $5f^{12}7p^1$, $5f^{12}7d^1$, $5f^{12}8s^1$, $5f^{12}8p^1$	59,898	213,624,256
Es II	$5f^{11}7s^1$, $5f^{11}6d^1$, $5f^{11}7p^1$, $5f^{10}6d^2$, $5f^{10}7s^2$, $5f^{10}6d^17s^1$, $5f^{10}6d^17p^1$, $5f^{10}7s^17p^1$, $5f^{11}7d^1$, $5f^{11}8s^1$, $5f^{11}8p^1$, $5f^{12}$	14,693	17,006,055
Es III	$5f^{11}$, $5f^{10}7s^1$, $5f^{10}6d^1$, $5f^{10}7p^1$	1,837	259,812
Es IV	$5f^{10}$, $5f^97s^1$, $5f^96d^1$, $5f^97p^1$	3,549	915,339
Fm I	$5f^{12}7s^2$, $5f^{11}6d^17s^2$, $5f^{11}6d^17s^17p^1$, $5f^{12}6d^17s^1$, $5f^{12}7s^17p^1$, $5f^{12}7s^17d^1$, $5f^{12}7s^18s^1$, $5f^{12}7s^18p^1$, $5f^{11}7s^27p^1$, $5f^{11}6d^27s^1$, $5f^{12}7p^2$, $5f^{12}6d^2$, $5f^{12}6d^17p^1$, $5f^{12}6d^17d^1$, $5f^{12}6d^18s^1$, $5f^{12}6d^18p^1$, $5f^{11}6d^27p^1$, $5f^{13}7s^1$, $5f^{13}6d^1$, $5f^{13}7p^1$, $5f^{13}7d^1$, $5f^{13}8s^1$, $5f^{13}8p^1$	21,847	28,998,514
Fm II	$5f^{12}7s^1$, $5f^{12}6d^1$, $5f^{12}7p^1$, $5f^{11}6d^2$, $5f^{11}7s^2$, $5f^{11}6d^17s^1$, $5f^{11}6d^17p^1$, $5f^{11}7s^17p^1$, $5f^{13}$, $5f^{12}7d^1$, $5f^{12}8s^1$, $5f^{12}8p^1$	5,535	2,629,353
Fm III	$5f^{12}$, $5f^{11}7s^1$, $5f^{11}6d^1$, $5f^{11}7p^1$	723	42,671
Fm IV	$5f^{11}$, $5f^{10}7s^1$, $5f^{10}6d^1$, $5f^{10}7p^1$	1,837	259,812
Md I	$5f^{13}7s^2$, $5f^{12}6d^17s^2$, $5f^{12}6d^17s^17p^1$, $5f^{13}6d^17s^1$, $5f^{13}7s^17p^1$, $5f^{13}7s^17d^1$, $5f^{13}7s^18s^1$, $5f^{13}7s^18p^1$, $5f^{12}7s^27p^1$, $5f^{13}7p^2$, $5f^{13}6d^17p^1$, $5f^{13}6d^17d^1$, $5f^{13}6d^18s^1$, $5f^{13}6d^18p^1$, $5f^{12}6d^27s^1$, $5f^{12}6d^27p^1$, $5f^{13}6d^2$, $5f^{14}7s^1$, $5f^{14}6d^1$, $5f^{14}7p^1$, $5f^{14}7d^1$, $5f^{14}8s^1$, $5f^{14}8p^1$	5,614	2,089,545
Md II	$5f^{13}7s^1$, $5f^{13}6d^1$, $5f^{13}7p^1$, $5f^{12}6d^2$, $5f^{12}7s^2$, $5f^{12}6d^17s^1$, $5f^{12}6d^17p^1$, $5f^{12}7s^17p^1$, $5f^{13}7d^1$, $5f^{13}8s^1$, $5f^{13}8p^1$, $5f^{14}$	1,521	216,741
Md III	$5f^{13}$, $5f^{12}7s^1$, $5f^{12}6d^1$, $5f^{12}7p^1$	202	3,797
Md IV	$5f^{12}$, $5f^{11}7s^1$, $5f^{11}6d^1$, $5f^{11}7p^1$	723	42,671
No I	$5f^{14}7s^17\ell^1$, $5f^{14}7s^18\ell^1$, $5f^{14}7s^19\ell^1$, $5f^{14}7s^110\ell^1$, $5f^{14}7s^111\ell^1$, $5f^{14}7s^112\ell^1$, $5f^{14}6d^17\ell^1$, $5f^{14}6d^18\ell^1$, $5f^{14}6d^19\ell^1$, $5f^{14}6d^110\ell^1$, $5f^{14}6d^111\ell^1$, $5f^{14}6d^112\ell^1$, $5f^{14}6d^16f^1$, $5f^{14}6d^16g^1$, $5f^{13}6d^17s^2$, $5f^{13}6d^27s^1$, $5f^{13}6d^17s^17p^1$, $5f^{13}7s^27p^1$, $5f^{13}7s^17p^2$, $5f^{13}6d^27p^1$, $5f^{13}7s^27d^1$, $5f^{14}7p^2$, $5f^{14}6d^2$, $5f^{13}6d^17p^2$	1,863	367,754
No II	$5f^{14}7\ell^1$, $5f^{14}8\ell^1$, $5f^{14}9\ell^1$, $5f^{14}6d^1$, $5f^{14}6f^1$, $5f^{14}6g^1$, $5f^{13}6d^2$, $5f^{13}7s^2$, $5f^{13}6d^17s^1$, $5f^{13}6d^17p^1$, $5f^{13}7s^17p^1$	292	10,037
No III	$5f^{14}$, $5f^{13}7s^1$, $5f^{13}6d^1$, $5f^{13}7p^1$, $5f^{13}7d^1$, $5f^{13}7f^1$, $5f^{13}6f^1$, $5f^{13}8s^1$, $5f^{13}8p^1$, $5f^{13}8d^1$, $5f^{13}8f^1$	171	3,192
No IV	$5f^{13}$, $5f^{12}7s^1$, $5f^{12}6d^1$, $5f^{12}7p^1$	202	3,797